Rank One Chaos in Switch-Controlled Murali-Lakshmanan-Chua Circuit

ALI OKSASOGLU*
Honeywell Corporation, 11100 N. Oracle Rd., Tucson, AZ 85737.

DONGSHENG MA†
Department of Electrical and Computer Engineering, The University of Arizona, Tucson, AZ 85721.

QIUDONG WANG‡
Department of Mathematics, The University of Arizona, Tucson, AZ 85721.

Abstract

In this paper, we investigate the creation of strange attractors in a switch-controlled MLC (Murali-Lakshmanan-Chua) circuit. The design and use of this circuit is motivated by a recent mathematical theory of rank one attractors developed by Wang and Young. Strange attractors are created by periodically kicking a weakly stable limit cycle emerging from the center of a supercritical Hopf bifurcation, and are found in numerical simulations by following a recipe-like algorithm. Rigorous conditions for chaos are derived and various switch control schemes, such as synchronous, asynchronous, single-, and multi-pulse, are investigated in numerical simulations.

*Email: ali.oksasoglu@honeywell.com.
†Email:ma@ece.arizona.edu
‡Email: dwang@math.arizona.edu. This research is partially supported by a grant from NSF.

1 Introduction

In this paper we continue our study on switch-controlled electrical circuits based on a new chaos theory of rank one maps developed recently by Wang and Young in [Wang & Young, 2001, 2004]. This new chaos theory originated from Jakobson's theory on unimodal maps [Jakobson, 1981] and the theory of Benedicks and Carleson's on strongly dissipative Hénon maps [Benedicks & Carleson, 1991]. The main result of this theory is as follows: for a given one parameter family f_a, $a \in I$ of rank one maps, i.e., maps with one direction of instability represented by 1-D functions with critical points, there is a set $\Delta \subset I$ of positive measure, such that $f_a, a \in \Delta$ admits homoclinc tangles without attracting periodic orbits (sinks). For a brief overview of this theory see [Wang & Oksasoglu, 2005]. Wang and Young also proved in [Wang & Young, 2002a,b] that, under the assumption that a given differential equation

$$\frac{d\mathbf{u}}{dt} = f(\mathbf{u}) \tag{1}$$

has a weakly stable periodic solution, the time-T map of the new equation

$$\frac{d\mathbf{u}}{dt} = f(\mathbf{u}) + \varepsilon\Phi(\mathbf{u})P_T(t) \tag{2}$$

obtained by adding a periodic forcing term $\varepsilon\Phi(\mathbf{u})P_T(t)$ of period T to Eq. (1) is a one parameter family of rank one maps in the neighborhood of the weakly stable periodic orbit of Eq. (1). This observation opened a door for the applications of this new chaos theory to real physical and engineering systems.

In [Oksasoglu *et al.*, 2005] we introduced periodically controlled switches as depicted in Fig. 1 to realize the general settings of Eq. (2). In this scheme, the state variables are modulated by externally controlled switches, and the control signals are

simply periodic pulse trains. When all switches are at their respective default positions (S1 at off position and S2 at position 2), the circuit behavior is represented by the autonomous system of Eq. (1). When the switches are turned to their alternative positions, specific non-autonomous terms are added as in Eq. (2). A switch-controlled Chua's circuit was studied in [Oksasoglu *et al.*, 2005].

In this investigation we study new realizations of the switch-controlled circuits. Each switch is again controlled externally by a periodic pulse train. By properly choosing the timings of the control pulses, we obtain various control scenarios. In particular, the scheme of Fig. 1 allows multi-pulse switch control. i.e., multiple kicks applied to one switch in one forcing period. We also adopt a new control scheme as depicted in Fig. 2 to allow multiple kicks of different magnitude. Note that in Fig. 2(b), it is assumed that whenever all the switches S_{2k} $(k \neq 0)$ are open, then S_{20} is closed. Note that the scheme of Fig. 1 is a special case of the scheme of Fig. 2.

These switch control schemes are applied to the second-order system shown in Fig. 3. This circuit is an autonomous version of the MLC (Murali-Lakshmanan-Chua) circuit [Murali *et al.*, 1994a,b] with the $v - i$ characteristics of the nonlinear resistor given by $i_n(v) = a_1 v + a_2 v^2 + a_3 v^3$. By applying the scheme of Fig. 2 to this second-order circuit, we obtain the switch-controlled circuit of Fig. 4. Studying this circuit from the perspective of the theory of rank one maps forms the subject of this paper. Essentially, we present a general scheme that can be potentially applied to transform any given circuit of weakly stable oscillations into a circuit of chaos. We start with the derivation of the differential equations for the circuit of Fig. 4 in Section 2. We then outline a recipe-like algorithm, which we will follow to find rank one chaos. Theoretical computations are presented in Section 2, and the results of numerical simulations are presented in Section 3.

2 Switch-controlled Circuit

2.1 Derivation of Equations

Our derivations are for the circuit depicted in Fig. 4 that allows for the switches to be controlled by multiple kicks of differing magnitudes. As shown in Fig. 4, there are seven switches in total, which we denote as S_{1k}, S_{20} and S_{2k}. Let s_{1k}, s_{2k}, $k = 1, 2, 3$ be the times at which S_{1k} and S_{2k} are to be turned on, respectively. Note that S_{20} is closed whenever all of S_{2k}, $k \neq 0$ are open. We assume that each periodic pulse train has the same period T_0, and the pulse-width p_0. For $k = 1, 2, 3$, S_{1k} is closed for $s_{1k} + nT_0 \leq t < s_{1k} + nT_0 + p_0$ (ON time), and is open elsewhere (OFF time) within a sigle period. Similarly, S_{2k} is closed for $s_{2k} + nT_0 \leq t < s_{2k} + nT_0 + p_0$ (ON time), and is open elsewhere (OFF time). We also assume that at any given time there is at most one switch (discounting the default switch S_{20}, of course) that is turned on. We have for $k = 1, 2, 3$,

$$\begin{aligned} C\frac{dv}{dt} &= i - f(v) - G_{1k}v \\ L\frac{di}{dt} &= -v - Ri \end{aligned} \tag{3}$$

if S_{1k} is turned on, and

$$\begin{aligned} C\frac{dv}{dt} &= i - f(v) \\ L\frac{di}{dt} &= -v - Ri - R_{2k}i \end{aligned} \tag{4}$$

if S_{2k} is turned on. If all switches (except S_{20}) are turned off, then

$$\begin{aligned} C\frac{dv}{dt} &= i - f(v) \\ L\frac{di}{dt} &= -v - Ri. \end{aligned} \tag{5}$$

Putting these equations together and assuming a three-pulse control signal, we obtain

$$
\begin{aligned}
C\frac{dv}{dt} &= i - f(v) - v\sum_{k=1}^{3}\sum_{n=0}^{\infty} G_{1k}F_{n,T_0,p_0,s_{1k}}(t) \\
L\frac{di}{dt} &= -v - Ri - i\sum_{k=1}^{3}\sum_{n=0}^{\infty} R_{2k}F_{n,T_0,p_0,s_{2k}}(t)
\end{aligned}
\tag{6}
$$

where

$$
F_{n,T_0,p_0,s_{jk}}(t) = \begin{cases} 1 & s_{jk} + nT_0 \le t < s_{jk} + nT_0 + p_0 \\ 0 & elsewhere. \end{cases}
\tag{7}
$$

By setting

$$
x = \frac{v}{V_0}, \quad y = \frac{i}{I_0}, \quad t \to \frac{t}{\omega_n},
$$

we obtain the following dimensionless set of equations

$$
\begin{aligned}
\frac{dx}{dt} &= \alpha[y - h(x)] - x\sum_{k=1}^{3}\varepsilon_{1k}P^{(1)}_{T,p,d_{1k}} \\
\frac{dy}{dt} &= -\beta[x + \gamma y] - y\sum_{k=1}^{3}\varepsilon_{2k}P^{(2)}_{T,p,d_{2k}}
\end{aligned}
\tag{8}
$$

where

$$
\begin{aligned}
P^{(j)}_{T,p,d_{jk}} &= \frac{1}{p}\sum_{n=0}^{\infty} F_{n,T,p,d_{jk}}; \\
d_{1k} &= s_{1k}\omega_n, \quad d_{2k} = s_{2k}\omega_n; \\
p &= p_0\omega_n, \quad T = T_0\omega_n, \ R_n = \frac{V_0}{I_0}; \\
h(x) &= b_1x + b_2x^2 + b_3x^3, \quad b_m = a_mR_nV_0^{m-1}; \\
\alpha &= \frac{1}{R_nC\omega_n}, \quad \beta = \frac{R_n}{L\omega_n}, \quad \gamma = \frac{R}{R_n}; \\
\varepsilon_{1k} &= \frac{G_{1k}p}{C\omega_n} = \frac{\alpha R_np}{R_{1k}}, \quad \varepsilon_{2k} = \frac{R_{2k}p}{L\omega_n} = \frac{\beta R_{2k}p}{R_n}
\end{aligned}
\tag{9}
$$

for $j = 1, 2,\ k, m = 1, 2, 3$. The general form of the resulting periodic pulse train in Eq. (8) for one period is depicted in Fig. 5.

2.2 A recipe-like algorithm for finding rank one chaos

The rest of this paper is devoted to the study of Eq. (8) regarding α, β, γ and $p, T, d_{ik}, \varepsilon_{ik}$ as parameters. Note that $\alpha, \beta, \gamma \in \mathbb{R}^+$. Although the theory of rank one attractors is mathematically involved, its application to systems of Eq. (2), hence to the switch-controlled circuits as in the schemes of Figs. 1 and 2 is relatively straight forward. The following procedure provides a *recipe* to create strange attractors in a given system of Eq. (1).

(a) Find a set of parameter values for a supercritical Hopf bifurcation with a weakly stable periodic solution emerging from the center of bifurcation.

(b) Compute the complex normal form for the flow on the central manifold for the Hopf bifurcation located in (a) up to the third order.

(c) Compute the ratio of the imaginary and the real parts of the leading degree three coeeficient of this normal form, the so called "twist constant", and find the values of parameters for which the twist constant is large in magnitude.

(d) Compute a function $\phi(\theta)$ defined on S^1 through a well-defined process (See [Wang & Oksasoglu, 2005]), and check that $\phi(\theta)$ so obtained is a Morse function. The rough geometric shape of the rank one attractors is determined by $\phi(\theta)$.

(e) Then the existence of rank one attractors is proved through Propositions 2.1 and 2.2 as stated in [Wang & Oksasoglu, 2005].

Note that (a)-(c) above are strictly on the autonomous part of Eq. (2), and (d) is determined by the forcing term. To find chaotic attractors in such circuits, it is crucial to find parameters values that will result in a large twist constant.

Let us also remark that, though the methods developed in [Wang & Young, 2002a,b] are in principle valid for systems employing multiple kicks, Propositions 2.1 and 2.2 in [Wang & Oksasoglu, 2005] apply only to the synchronous, single-pulse case, for which we set

$$\begin{aligned} d_{1k} = d_{2k} = 0, \quad k = 1, 2, 3 \\ \varepsilon_{1k} = \varepsilon_{2k} = 0, \quad k = 2, 3. \end{aligned} \tag{10}$$

In this case, the set of equations is given by

$$\begin{aligned} \frac{dx}{dt} &= \alpha[y - h(x)] - \varepsilon_{11} x P_{T,p,0} \\ \frac{dy}{dt} &= -\beta[x + \gamma y] - \varepsilon_{11} y \frac{\varepsilon_{21}}{\varepsilon_{11}} P_{T,p,0}. \end{aligned} \tag{11}$$

2.3 Hopf Bifurcation and Normal Forms

We can rewrite Eq. (11) as

$$\frac{d}{dt}\begin{bmatrix} x \\ y \end{bmatrix} = \begin{bmatrix} -\alpha b_1 & \alpha \\ -\beta & -\beta\gamma \end{bmatrix}\begin{bmatrix} x \\ y \end{bmatrix} + \begin{bmatrix} -b_2\alpha x^2 - b_3\alpha x^3 \\ 0 \end{bmatrix} + \varepsilon_{11}\begin{bmatrix} -x \\ -\frac{\varepsilon_{21}}{\varepsilon_{11}} y \end{bmatrix} P_{T,p,0}(t). \tag{12}$$

Let us for the moment fix the values of α, b_1, β and regard γ as a parameter of bifurcation. It follows from a straight forward computation that, at

$$\gamma_0 = -\frac{\alpha b_1}{\beta} > 0, \tag{13}$$

the eigenvalues of the linear part of Eq. (12) are purely imaginary, and a supercritical Hopf bifurcation occurs at $(x, y) = (0, 0)$ for the autonomous system obtained by setting $\varepsilon_{11} = \varepsilon_{21} = 0$ in Eq. (12) (which corresponds to keeping the switches in Fig. 4 in their off or default positions at all times). It follows that the eigenvalues of the linear part of Eq. (12) are $\sigma \pm i\omega$ with

$$\sigma = -\frac{1}{2}(\alpha b_1 + \beta\gamma), \qquad \omega^2 = \alpha\beta - \frac{1}{4}(\alpha b_1 - \beta\gamma)^2. \tag{14}$$

From Eq. (14), we have at $\gamma = \gamma_0$,

$$\sigma = 0, \quad \omega^2 = \alpha(\beta - \alpha b_1^2) > 0 \tag{15}$$

which implies that

$$b_1 \in (-\sqrt{\frac{\beta}{\alpha}}, 0). \tag{16}$$

To convert the linear part of Eq. (12) into the standard Jordan form we let

$$\begin{bmatrix} x \\ y \end{bmatrix} = \begin{bmatrix} 1 & 0 \\ b_1 + \frac{\sigma}{\alpha} & -\omega/\alpha \end{bmatrix} \begin{bmatrix} \xi \\ \eta \end{bmatrix}. \tag{17}$$

In terms of the new variables ξ and η, Eq. (12) becomes

$$\begin{aligned} \frac{d\xi}{dt} &= \sigma\xi - \omega\eta - \alpha(b_2\xi^2 + b_3\xi^3) - \varepsilon_{11}\xi P_{T,p,0}(t) \\ \frac{d\eta}{dt} &= \omega\xi + \sigma\eta - \frac{\alpha(\sigma + \alpha b_1)}{\omega}(b_2\xi^2 + b_3\xi^3) + \varepsilon_{11}[\frac{\sigma + b_1\alpha}{\omega}(\frac{\varepsilon_{21}}{\varepsilon_{11}} - 1)\xi - \frac{\varepsilon_{21}}{\varepsilon_{11}}\eta]P_{T,p,0}(t). \end{aligned} \tag{18}$$

Next, we rewrite Eq. (18) in a complex variable $z = \xi + i\eta$ and derive a normal

form for its autonomous part in z. From $z = \xi + i\eta$, $\bar{z} = \xi - i\eta$, we have

$$\xi = \frac{1}{2}(z + \bar{z}), \qquad \eta = \frac{1}{2i}(z - \bar{z}). \tag{19}$$

We obtain from Eq. (18) that

$$\frac{dz}{dt} = (\sigma + i\omega)z - \frac{\alpha}{8}[1 + i\frac{\sigma + b_1\alpha}{\omega}][2b_2(z + \bar{z})^2 + b_3(z + \bar{z})^3] \tag{20}$$

According to the standard normal form theory, there exists a change of variables near identity, which we write as

$$z = Z + c_2 Z^2 + c_3 Z^3 + \cdots , \tag{21}$$

that transfers Eq. (20) to

$$\frac{dZ}{dt} = (\sigma + i\omega)Z + k_1 Z^2 \bar{Z} + \mathcal{O}(|Z|^5) \tag{22}$$

where the term$\mathcal{O}(|Z|^n)$ represents the terms of magnitude $< K|Z|^n$ in a sufficiently small neighborhood of $Z = 0$ for some constant K. Using the formula given in [Guckenheimer & Holmes, 1997], we have

$$k_1 = \frac{i}{2\omega}(h_{zz}h_{z\bar{z}} - 2|h_{z\bar{z}}|^2 - \frac{1}{3}|h_{\bar{z}\bar{z}}|^2) + \frac{1}{2}h_{zz\bar{z}} \tag{23}$$

where, in our case,

$$
\begin{aligned}
h_{zz} &= -\frac{\alpha b_2}{2}[1 + i\frac{\sigma + b_1\alpha}{\omega}] \\
h_{z\bar{z}} &= -\frac{\alpha b_2}{2}[1 + i\frac{\sigma + b_1\alpha}{\omega}] \\
h_{\bar{z}\bar{z}} &= -\frac{\alpha b_2}{2}[1 + i\frac{\sigma + b_1\alpha}{\omega}] \\
h_{zz\bar{z}} &= -\frac{3\alpha b_3}{4}[1 + i\frac{\sigma + b_1\alpha}{\omega}]
\end{aligned}
\tag{24}
$$

are the normalized coefficients of the terms z^2, $z\bar{z}$, $\bar{z}\bar{z}$ and $zz\bar{z}$ on the right hand side of Eq. (20), respectively. By a straight forward computation, we obtain

$$
\begin{aligned}
Re(k_1) &= -\frac{\alpha}{8\omega^2}[2\alpha^2 b_2^2(b_1 + \sigma/\alpha) + 3b_3\omega^2] \\
Im(k_1) &= -\frac{\alpha^2}{24\omega^3}\left[(b_1 + \sigma/\alpha)(9b_3\omega^2 + 10\alpha^2 b_2^2(b_1 + \sigma/\alpha)) + 4b_2^2\omega^2\right].
\end{aligned}
\tag{25}
$$

Remark: (1) According to the standard theory of Hopf bifurcations, a periodic solution emerges from $Z = 0$ when the value of γ passes γ_0 in Eq. (12) provided that $Re(k_1) \neq 0$. Furthermore, the emerging periodic solution is asymptotically stable if $Re(k_1) < 0$, and asymptotically unstable if $Re(k_1) > 0$. In this paper, we are only interested in the asymptotically stable case. Thus, from Eq. (25), we have the following stability criterion:

$$
2\alpha^2 b_2^2(b_1 + \sigma/\alpha) + 3b_3\omega^2 > 0. \tag{26}
$$

(2) Note that we have, at $\gamma = \gamma_0$,

$$
\begin{aligned}
Re(k_1) &= \frac{-\alpha}{8(\beta - \alpha b_1^2)}[2\alpha b_2^2 b_1 + 3b_3(\beta - \alpha b_1^2)] \\
Im(k_1) &= -\frac{\alpha^2}{24\omega(\beta - \alpha b_1^2)}[10\alpha^2 b_2^2 b_1^2 + (\beta - \alpha b_1^2)(4b_2^2 + 9b_1 b_3)],
\end{aligned}
\tag{27}
$$

and the stability condition of Eq. (26) becomes

$$2\alpha^2 b_2^2 b_1 + 3b_3\alpha(\beta - \alpha b_1^2) > 0. \tag{28}$$

(3) Let us also note that, at $\gamma = \gamma_0$ we have

$$\left|\frac{Im(k_1)}{Re(k_1)}\right| = \frac{\alpha}{3\omega}\left|\frac{[10\alpha^2 b_2^2 b_1^2 + (\beta - \alpha b_1^2)(4b_2^2 + 9b_1 b_3)]}{2\alpha b_2^2 b_1 + 3b_3(\beta - \alpha b_1^2)}\right|. \tag{29}$$

This ratio is the so-called twist constant the magnitude of which needs to be large for chaotic attractors to exist.

(4) As the last step, we need to compute $\phi(\theta)$. Following the notation of [Wang & Oksasoglu, 2005], we have

$$\begin{aligned} \Phi_\xi &= -\xi \\ \Phi_\eta &= \frac{\sigma + b_1\alpha}{\omega}(\frac{\varepsilon_{21}}{\varepsilon_{11}} - 1)\xi - \frac{\varepsilon_{21}}{\varepsilon_{11}}\eta. \end{aligned} \tag{30}$$

Let

$$\xi = \cos\theta,\ \ \eta = \sin\theta. \tag{31}$$

We have

$$\begin{aligned} \phi(\theta) &= \cos\theta\Phi_\xi + \sin\theta\Phi_\eta \\ &= -\cos^2\theta + (\frac{\sigma + \alpha b_1}{\omega})(\frac{\varepsilon_{21}}{\varepsilon_{11}} - 1)\cos\theta\sin\theta - \frac{\varepsilon_{21}}{\varepsilon_{11}}\sin^2\theta. \end{aligned} \tag{32}$$

$\phi(\theta)$ is indeed a Morse function.

3 Numerical Simulations: Observable Chaos

3.1 Initial Choice of Parameter Values

In this section, we present pictures of chaotic attractors obtained by numerical simulations. Our simulations are performed using the fourth-order Runge-Kutta routine starting at $t_0 = 0$. The parameters $\alpha = 10, \beta = 1, \gamma = 0.99, b_1 = -0.1, b_2 = 1.165, b_3 = 1$ are fixed throughout. With these parameter values we are close to a Hopf bifurcation (appears at $\gamma_0 = 1$) with a relatively large twist constant (≈ 2850). Computations performed earlier in Section 2 on the parameters of Hopf bifurcations and on the twist constant are instrumental for our choice of these parameter values. Our main considerations are to be reasonably close to a point of supercritical Hopf bifurcation, and to have a relatively large twist constant. There is nothing more that is intentional in our specification of these parameter values.

In all cases, we let p, the length of time the switches are on, be fixed at $p = 0.5$. For each picture presented, one discrete orbit starting near the attractor of the time-T map is plotted. With the parameter values specified as above, the things left for us to vary at the moment are (i) the forcing period T, (ii) the magnitude of the kicks in one period (ε_{ik}), and (iii) the times the kicks are initiated (d_{ik}). To further remove (iii) from this list of uncertainties we set $d_{11} = 0$, $d_{12} = 50$, $d_{13} = 85$, $d_{21} = 25$, $d_{22} = 110$, $d_{23} = 130$ throughout. These specific choices for d_{ik} are rather arbitrary but the unevenness in the spacing of consecutive pulses is intentional.

The weakly stable limit cycle, obtained by setting all $\varepsilon_{ik} = 0$, is depicted in Fig. 5. This limit cycle is then kicked periodically to create various pictures of chaos.

3.2 Observable Chaos: Multiple Kicks of the Same Magnitude

For the simulations of this subsection, ε_{ik} is either 0.32 or 0. In this case the circuit is controlled by the simpler scheme of Fig. 1. We are free to take away any one of the six potential kicks by setting its corresponding magnitude to 0. Figures 7-11 are a set of pictures of chaotic attractors obtained by numerical simulations. These pictures are presented in the ascending order in the number of kicks involved (from one to six). The geometric complexity of the chaotic attractors appears to increase as more kicks are employed within one period.

Observe that, for the simulations presented above, the length of the last relaxation interval, i.e., the time from the last kick in one forcing period to the end of the same forcing period, is not very long. Consequently, the rank one character present in these pictures through a rotating feature in angular direction, is not yet dominating. In Figs. 13 and 14, the forcing period is appropriately increased, and the structure of the attractors in radial direction is compressed. Figure 13 is the correspondence of Fig. 7 with one kick, and Fig. 14 is that of Fig. 12 with six kicks. In Fig. 15, the length of the forcing period is further increased. With very long relaxation periods, the attractor is pressed down in the radial direction, getting the look of a simple curve. Fig. 15 is, however, a picture of a chaotic attractor of extreme complexity but it is compressed very thin. A locally magnified picture of Fig. 15 is shown in Fig. 16. Figure 15 is an example of a true rank one attractor proved to exist by the theory of rank one maps and the computations of Section 2.

3.3 Observable Chaos: Multiple Kicks of Varying Magnitudes

In this subsection we present pictures of chaotic attractors allowing multiple kicks of different magnitude. All parameters except ε_{ik} and T are the same as in the last subsection. We set $\varepsilon_{1k} = 0.22$, $\varepsilon_{2k} = 0.12$ for Fig. 17. Here the circuit is still controlled by two switches according to the scheme of Fig. 1, each admitting three impulses in one forcing period. To adjust ε_{1k} and ε_{2k} we adjust the values of R_1 and R_2 in Fig. 1 as given by Eq. (9). For Fig. 18, $\varepsilon_{1k} = 0.12$, $\varepsilon_{2k} = 0.22$. The differences in these two pictures are caused by swapping the magnitudes of the control pulses. $T = 155.0$ and $T = 155.5$ are used for Fig. 17 and Fig. 18, respectively.

Figure 19 is obtained by changing ε_{12} for Fig. 18 from 0.12 to 0.52. For Fig. 19 we need the switch network of Fig. 2(a). Fig. 20 is obtained by further changing ε_{23} for Fig. 19 from 0.22 to 0.42. The switch network of Fig. 2(b) is used for the circuit of Fig. 20. $T = 167.5$ and $T = 168.5$ are used for Fig. 19 for Fig. 20, respectively. Finally, for Fig. 21 we use the full design of Fig. 4 by letting $\varepsilon_{11} = 0.32$, $\varepsilon_{12} = 0.52$, $\varepsilon_{13} = 0.12$, $\varepsilon_{21} = 0.22$, $\varepsilon_{22} = 0.32$, $\varepsilon_{23} = 0.42$. $T = 217$ is used for Fig. 21. These pictures do indicate that utilizing kicks of varying magnitudes does contribute in generating chaotic attractors of interesting geometric structure.

Note that in favor of getting chaotic pictures of complicated structure, the forcing periods are intentionally set short to minimize the compressing effect in the radial direction. By making T larger, rank one character for these chaotic attractors becomes more dominating. Figures 22 and 23 are the respective correspondences of Fig. 21 for $T = 270.5$ and $T = 470$.

3.4 Sensitive Dependency on Parameters, Robustness and Transient Chaos

A. *Sensitive dependency on parameters*

Figures 7-23 are pictures of **observable chaos**. They are pictures of homoclinic tangles without attracting periodic orbits. Unlike uniformly hyperbolic systems, the geometric and dynamical structures of observable chaos are, in general, not stable. For a typical one parameter family of rank one maps, the set of parameters for observable chaos is typically nowhere dense on any given interval of parameters. For example, let us fix the values of all parameters other than T for the solutions of Eq. (8), and regard the time-T map F_T as a one parameter family. Then the pictures of chaos are not robust in the sense that they often give way to pictures of sinks under small perturbations of T. See Figs. 24 and 25. For Fig. 24, $\varepsilon_{1k} = \varepsilon_{2k} = 0.12$, $T = 166$. Fig. 25 is obtained by varying the value of T for Fig. 22 from $T = 166$ to $T = 165.5$. See [Wang & Oksasoglu, 2005] and [Oksasoglu *et al.*, 2005] for a complete discussion on observable chaos and tangles dominated by sinks.

B. *Robustness of observable chaos*

Since the set of parameters for observable chaos is in general nowhere dense, these parameter values can not be accurately determined with finite precision, as unfortunately being always the case in numerical simulations. This is obviously a problem of practical consequences. A question one may naturally ask is how to associate results of simulations and experiences to the real physical process in the presence of such uncertainty. To this question the answer given by the theory of rank one attractors is as follows. We know that, for a given interval of parameters, the set of parameters for observable chaos is of **positive** measure, implying that, by randomly experimenting on this interval, one would hit observable chaos with

positive probability. We would have a high probability of hitting observable chaos if the measure for the set of good parameters (parameters of observable chaos) is relatively large, otherwise our chance would be slim.

For the time-T maps studied in this paper, the measure of good parameters are relatively large around parameter values of large twist constant according to the theory established in [Wang & Young, 2002a,b]. This is the reason why the explicit computation of twist constant in Section 2 are crucial for us. Our chance of hitting pictures of observable chaos diminishes rather quickly with parameters of smaller twist constant. By changing the value of b_2 from 0.165 to 0.12, for instance, the twist constant changes from ≈ 2850 to ≈ 27. Consequently, our chance of hitting observable chaos is greatly reduced. This prediction of theory is in perfect consistency with our simulation results. With $b_2 = 0.165$, we hit observable chaos all the time. However, for $b_2 = 0.12$ and with the same ε_{ik}, pictures of observable chaos become much harder to find. Our experience also indicates that multiple kicks of different magnitudes increase our chance of hitting observable chaos. As we have seen in the pictures presented in the last subsection, a combination of a reasonably large twist constant and multiple kicks of different magnitudes is a good recipe that generates consistent pictures of observable chaos of various geometrical and dynamical structure.

C. *Transient chaos and additional pitfalls*

The two main scenarios we have encountered so far, i.e., tangles without sinks and tangles with a dominating sink, are the extreme cases in terms of chaotic and stable asymptotic behavior for the circuit we study. In principle, there should also be intermediate cases of mixed behavior not yet accessible for rigorous analysis. One conceivable scenario is the co-existence of a sink side by side with a chaotic attractor of a basin of positive Lebesgue measure. These possible intermediate scenarios are probable explanations for pictures of *transient chaos* we occasionally encounter in

numerical simulation. These are instances of simulations in which the depicted orbit first appears to give a picture of observable chaos for a long stretch of time, then suddenly becomes periodic. Figure 26 provides a good example. In Fig. 26, the picture looks perfectly chaotic up to the time $\approx 2000 \times T$. The orbit we depict, however, suddenly changes to become periodic afterwards. We would also like to caution that, in eye-spotting observable chaos, the time-T map, not the continuous solutions in phase space, is strongly preferred. Figure 27 shows the two respective plots of the continuous solutions from Figs. 24 and 25. They do not look very different from each other.

4 Conclusion

In this paper we continued our study on chaotic attractors generated by switch-controlled electrical circuits. What we have proposed so far in our studies is a general switch control scheme that can be potentially applied to transform any given nonlinear circuit of weakly stable oscillations to a circuit of chaos. The specific second-order circuit used in this study is based on the MLC (Murali-Lakshmanan-Chua) circuit. The autonomous part of the MLC circuit is basically retained, but modified in such a way to modulate the capacitor voltage and the inductor current with a periodic pulse train. This modulation scheme is accomplished by using externally controlled switches. Then, the resulting system is studied following a recipe-like procedure that is designed based on a recent theory of rank one maps. In addition to the derivation of rigorous conditions for chaos, various switch control schemes, such as synchronous, asynchronous, single-, and multi-pulse, are investigated in numerical simulations. Multiple kicks of different magnitudes are also employed in one forcing period to generate strange attractors of various geometric and dynamical structures. The is-

sues considered also include sensitive dependency of chaotic attractors on parameters, robustness of observable chaos and transient chaos.

References

Benedicks, M. & Carleson, L. [1991] "The dynamics of the Hénon map," *Ann. Math.* **133**, 73–169.

Guckenheimer, J. & Holmes, P. [1997] *Nonlinear Oscillations , Dynamical Systems and Bifurcations of Vector Fields* page 155 Applied Mathematical Sciences. Springer-Verlag New York fifth edition.

Jakobson, M. [1981] "Absolutely continues invariant measures for one-parameter families of one-dimensional maps," *Commun. Math. Phys.* **81**, 39–88.

Murali, K., Lakshmanan, M., & Chua, L. O. [1994a] "Bifurcation and chaos in the simplest dissipative nonautonomous circuit," *Int. J. Bifurc. Chaos* **4**(6), 1511–1524.

Murali, K., Lakshmanan, M., & Chua, L. O. [1994b] "The simplest dissipative nonautonomous chaotic circuit," *IEEE Trans. Circuits Syst. I* **41**(6), 462–463.

Oksasoglu, A., Ma, D., & Wang, Q. [2005] "Observable chaos in switch-controlled chua's circuit," *Submitted to IEEE Trans. Circuits Syst. I.*

Wang, Q. & Oksasoglu, A. [2005] "Strange attractors in periodically kicked Chua's circuit," *Int. J. Bifurc. Chaos* **16**(1), 000–000.

Wang, Q. & Young, L.-S. [2001] "Strange attractors with one direction of instability," *Commun. Math. Phys.* **218**, 1–97.

Wang, Q. & Young, L.-S. [2002a] "From invariant curves to strange attractors," *Commun. Math. Phys.* **225**, 275–304.

Wang, Q. & Young, L.-S. [2002b] "Strange attractors in periodically-kicked limit cycles and Hopf bifurcations," *Commun. Math. Phys.* **240**, 509–529.

Wang, Q. & Young, L.-S. [2004] "Toward a theory of rank-one attractors," *In preprint.*

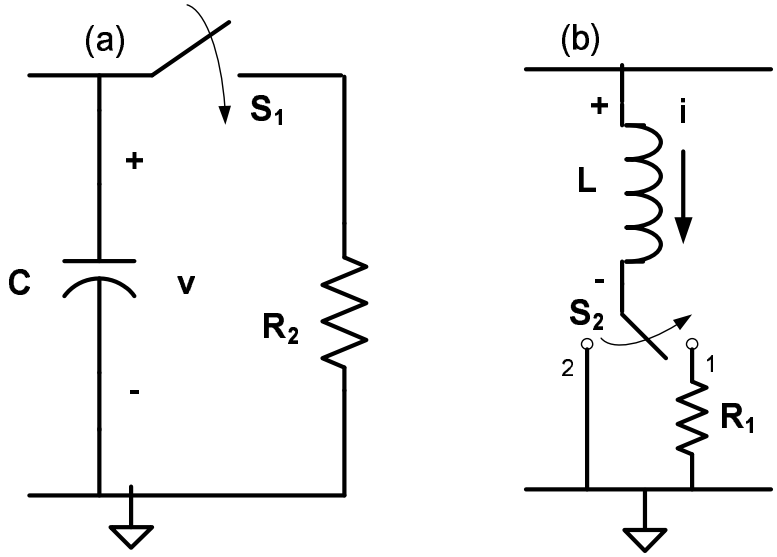

Figure 1: A switch control scheme for employing multiple kicks of same magnitude.

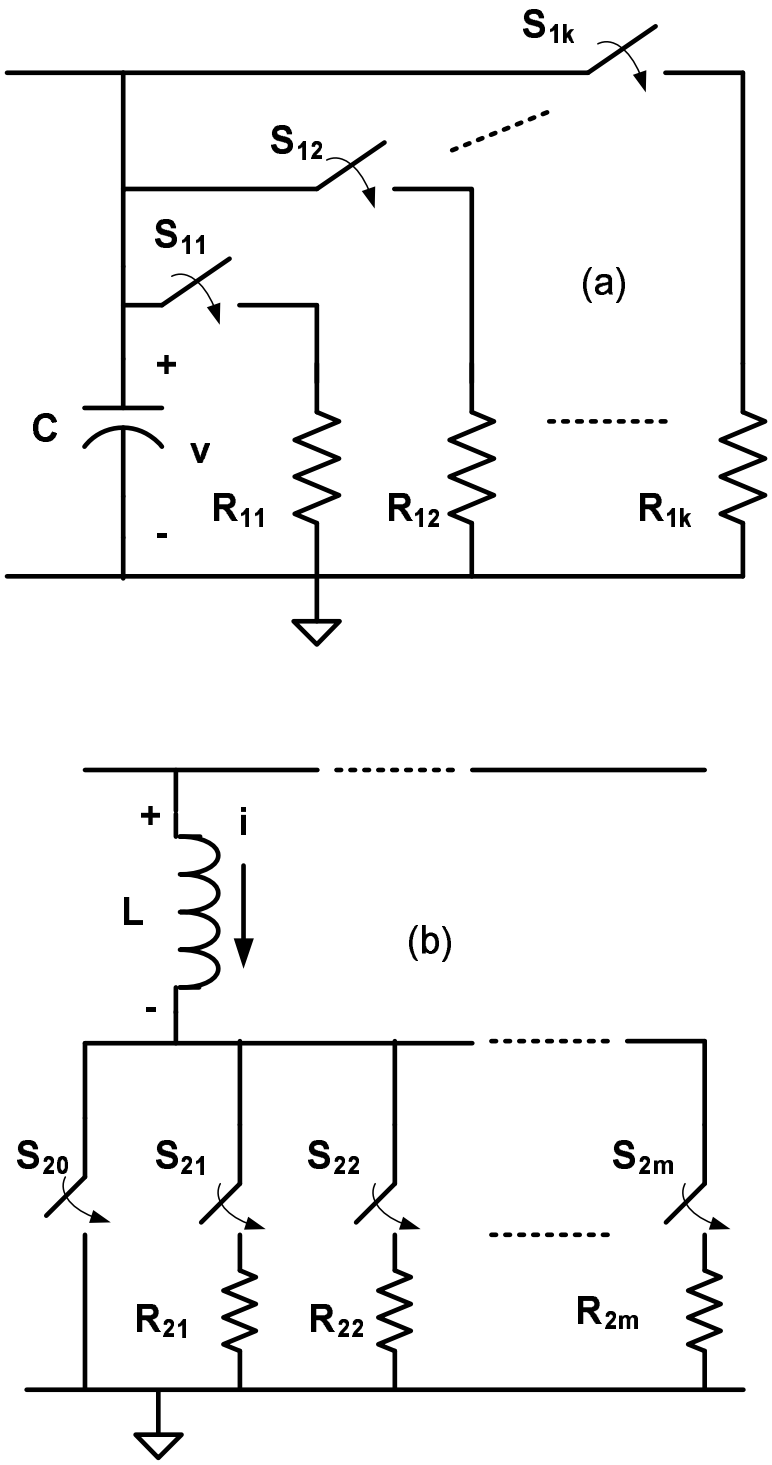

Figure 2: A switch control scheme for employing multiple kicks of different magnitude.

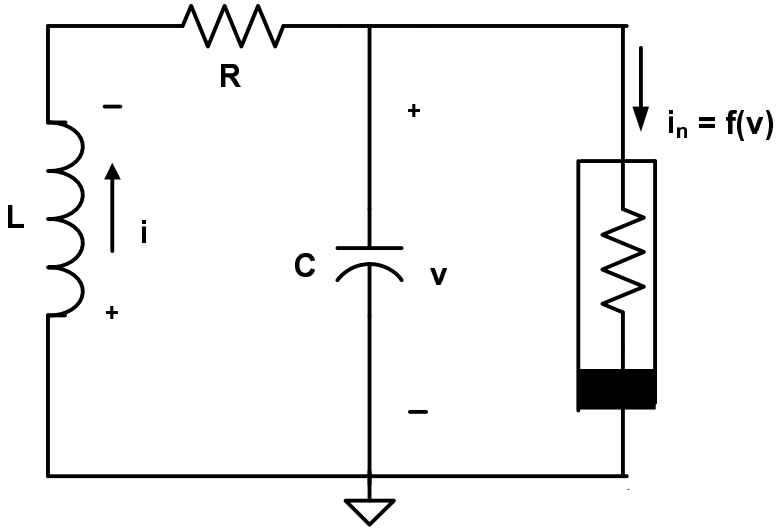

Figure 3: A second-order autonomous circuit.

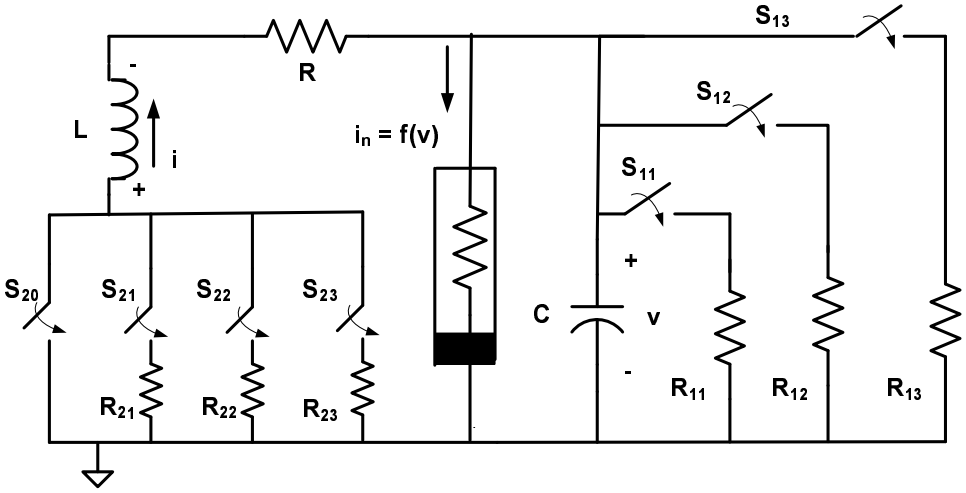

Figure 4: Switch-controlled circuit based on different magnitude, multi-pulse control scheme.

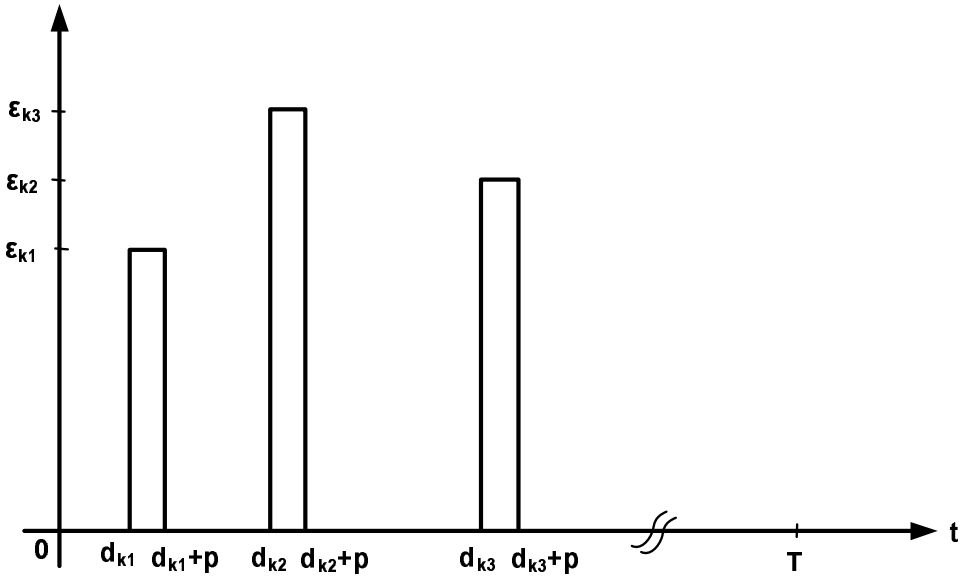

Figure 5: Periodic Pulse Train Generating Multiple Kicks of Different Magnitude.

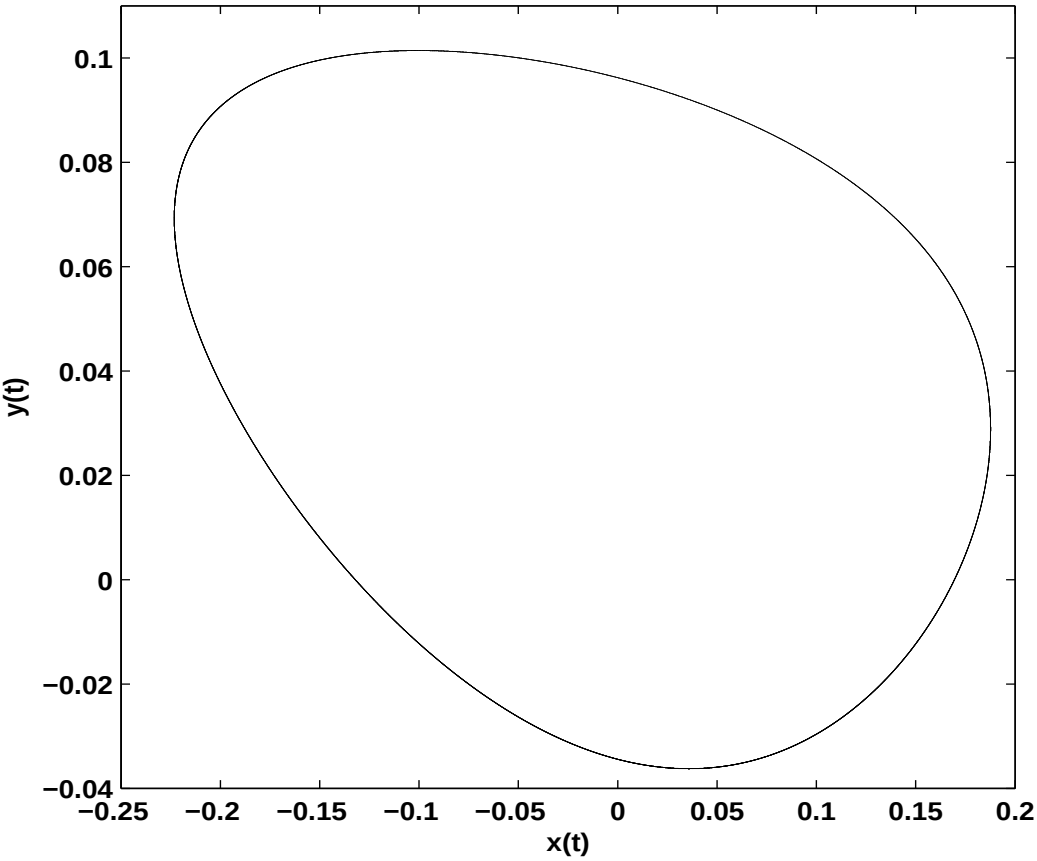

Figure 6: A Hopf Limit cycle ($\varepsilon = 0$).

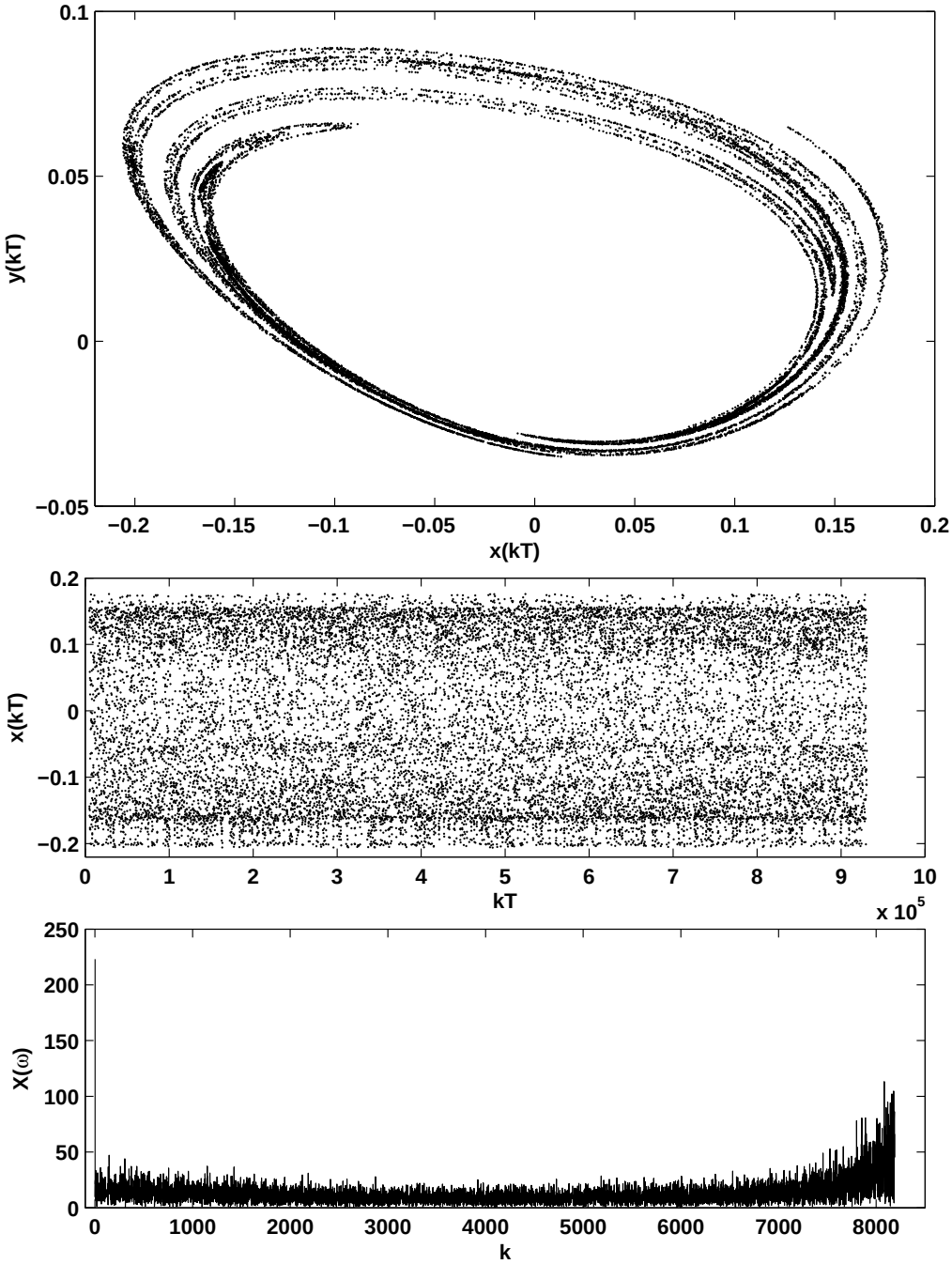

Figure 7: Strange attractor, $T = 56.5, \varepsilon_{11} = 0.32, \varepsilon_{12} = \varepsilon_{13} = \varepsilon_{21} = \varepsilon_{22} = \varepsilon_{23} = 0$. Time-T map (top), $x(kT)$ versus kT (middle), frequency spectrum of $x(kT)$ (bottom).

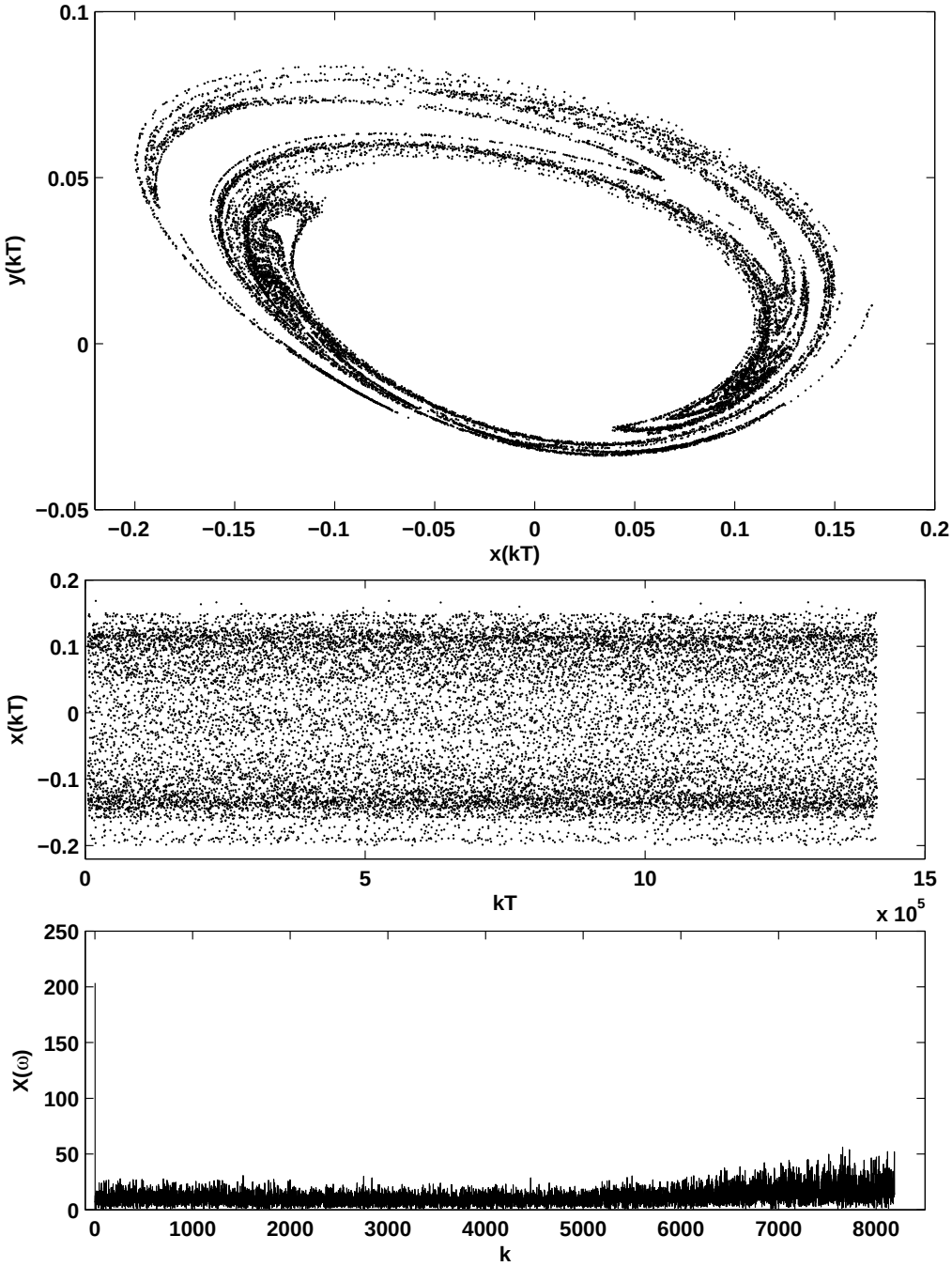

Figure 8: Strange attractor, $T = 86.0, \varepsilon_{11} = \varepsilon_{12} = 0.32, \varepsilon_{13} = \varepsilon_{21} = \varepsilon_{22} = \varepsilon_{23} = 0$. Time-T map (top), $x(kT)$ versus kT (middle), frequency spectrum of $x(kT)$ (bottom).

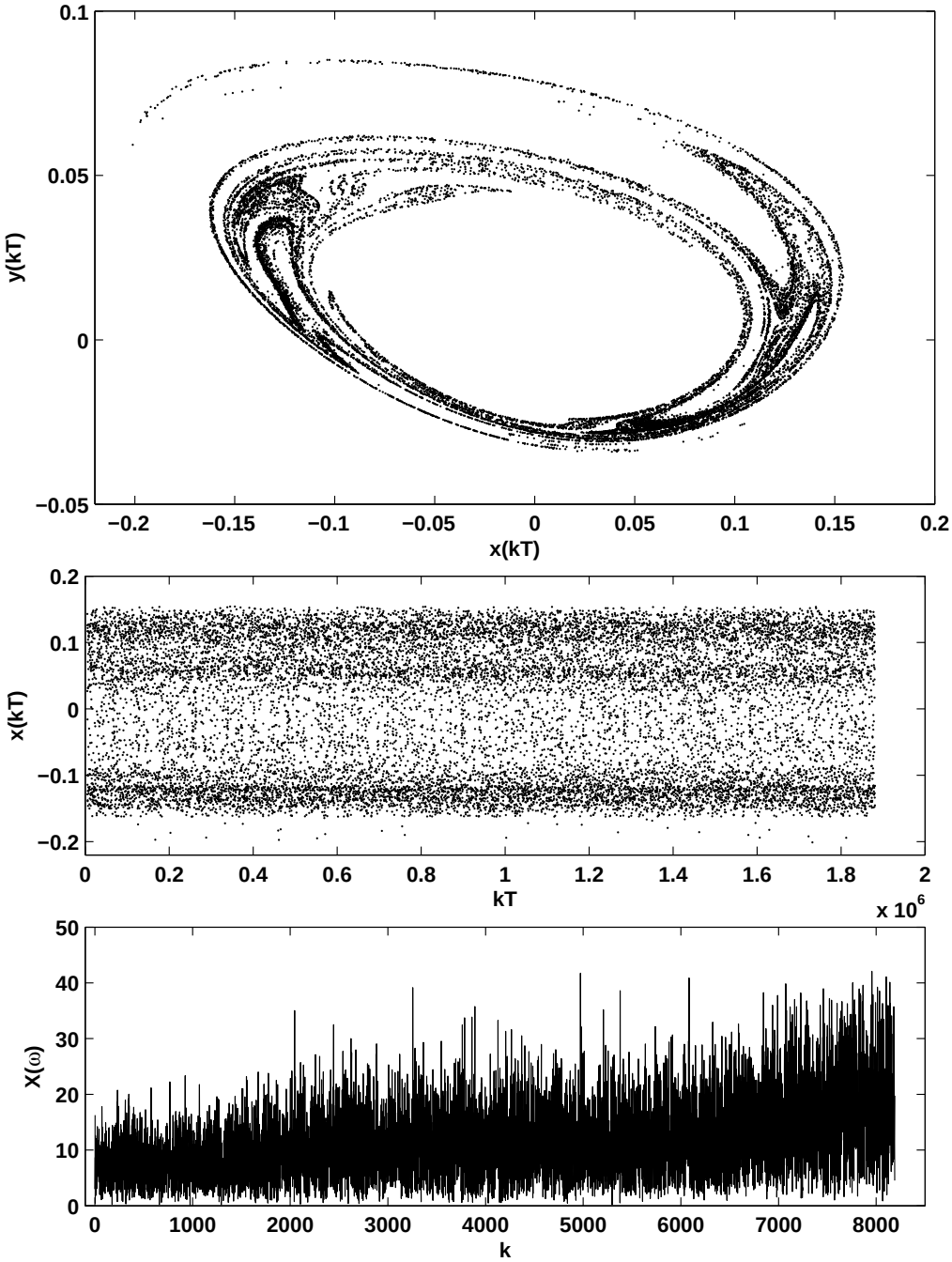

Figure 9: Strange attractor, $T = 114.5, \varepsilon_{11} = \varepsilon_{12} = \varepsilon_{13} = 0.32, \varepsilon_{21} = \varepsilon_{22} = \varepsilon_{23} = 0$. Time-T map (top), $x(kT)$ versus kT (middle), frequency spectrum of $x(kT)$ (bottom).

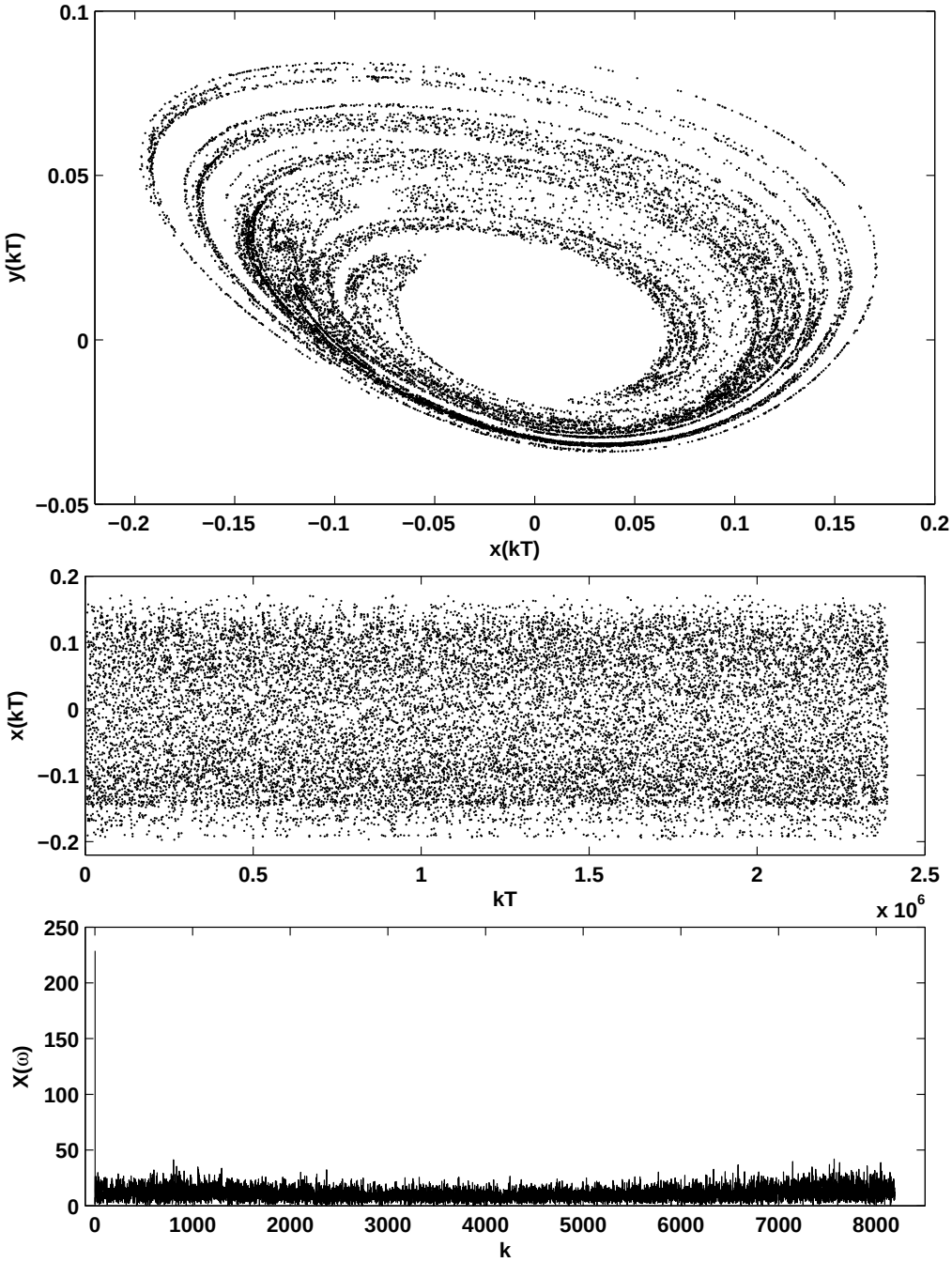

Figure 10: Strange attractor, $T = 145.5, \varepsilon_{11} = \varepsilon_{12} = \varepsilon_{13} = \varepsilon_{21} = 0.32, \varepsilon_{22} = \varepsilon_{23} = 0$. Time-T map (top), $x(kT)$ versus kT (middle), frequency spectrum of $x(kT)$ (bottom).

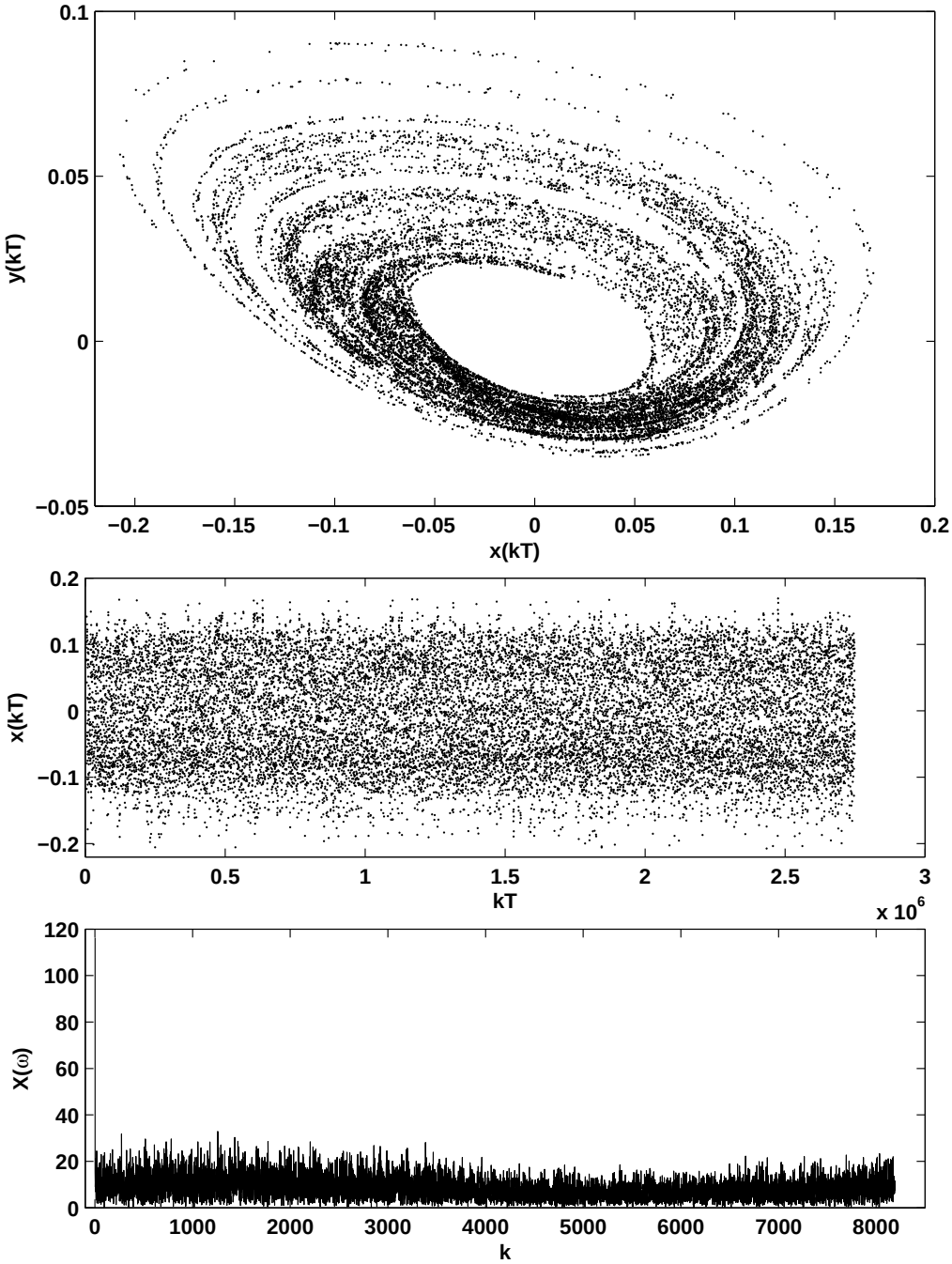

Figure 11: Strange attractor, $T = 167.5, \varepsilon_{11} = \varepsilon_{12} = \varepsilon_{13} = \varepsilon_{21} = \varepsilon_{22} = 0.32, \varepsilon_{23} = 0$. Time-T map (top), $x(kT)$ versus kT (middle), frequency spectrum of $x(kT)$ (bottom).

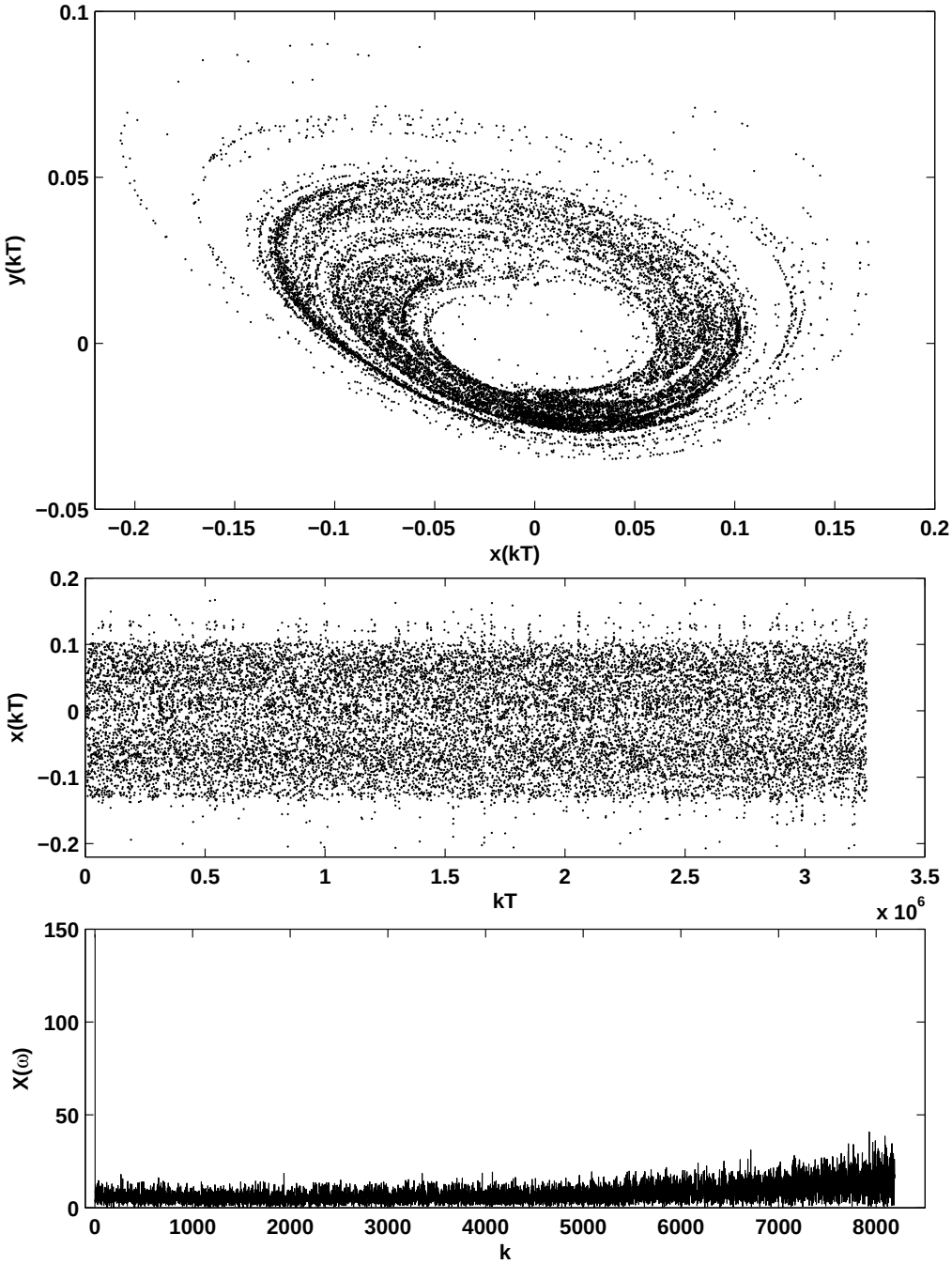

Figure 12: Strange attractor, $T = 198.5, \varepsilon_{11} = \varepsilon_{12} = \varepsilon_{13} = \varepsilon_{21} = \varepsilon_{22} = \varepsilon_{23} = 0.32$. Time-T map (top), $x(kT)$ versus kT (middle), frequency spectrum of $x(kT)$ (bottom).

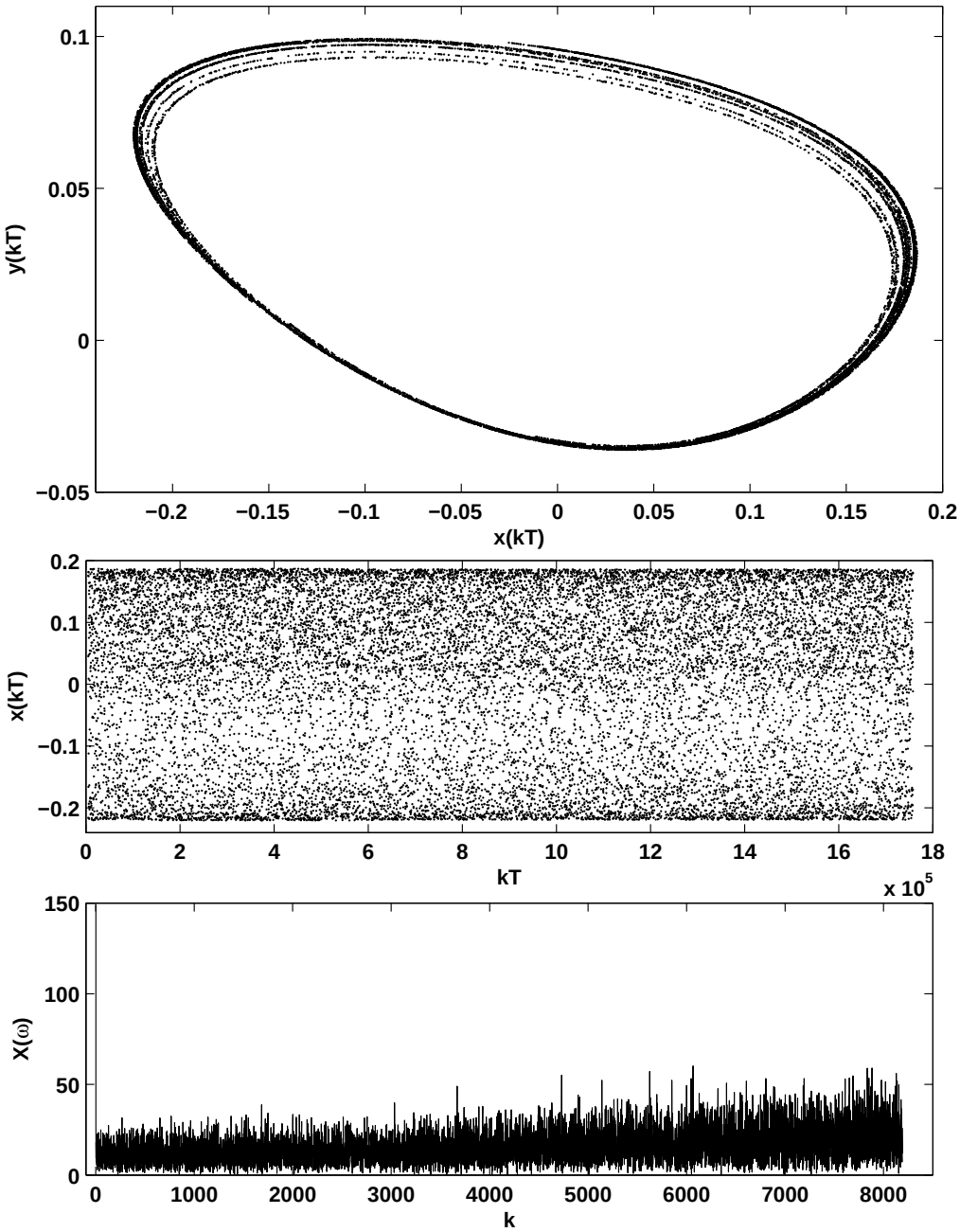

Figure 13: Strange attractor, $T = 107.0, \varepsilon_{11} = 0.32, \varepsilon_{12} = \varepsilon_{13} = \varepsilon_{21} = \varepsilon_{22} = \varepsilon_{23} = 0$. Time-T map (top), $x(kT)$ versus kT (middle), frequency spectrum of $x(kT)$ (bottom).

Figure 14: Strange attractor, $T = 267.5, \varepsilon_{11} = \varepsilon_{12} = \varepsilon_{13} = \varepsilon_{21} = \varepsilon_{22} = \varepsilon_{23} = 0.32$. Time-T map (top), $x(kT)$ versus kT (middle), frequency spectrum of $x(kT)$ (bottom).

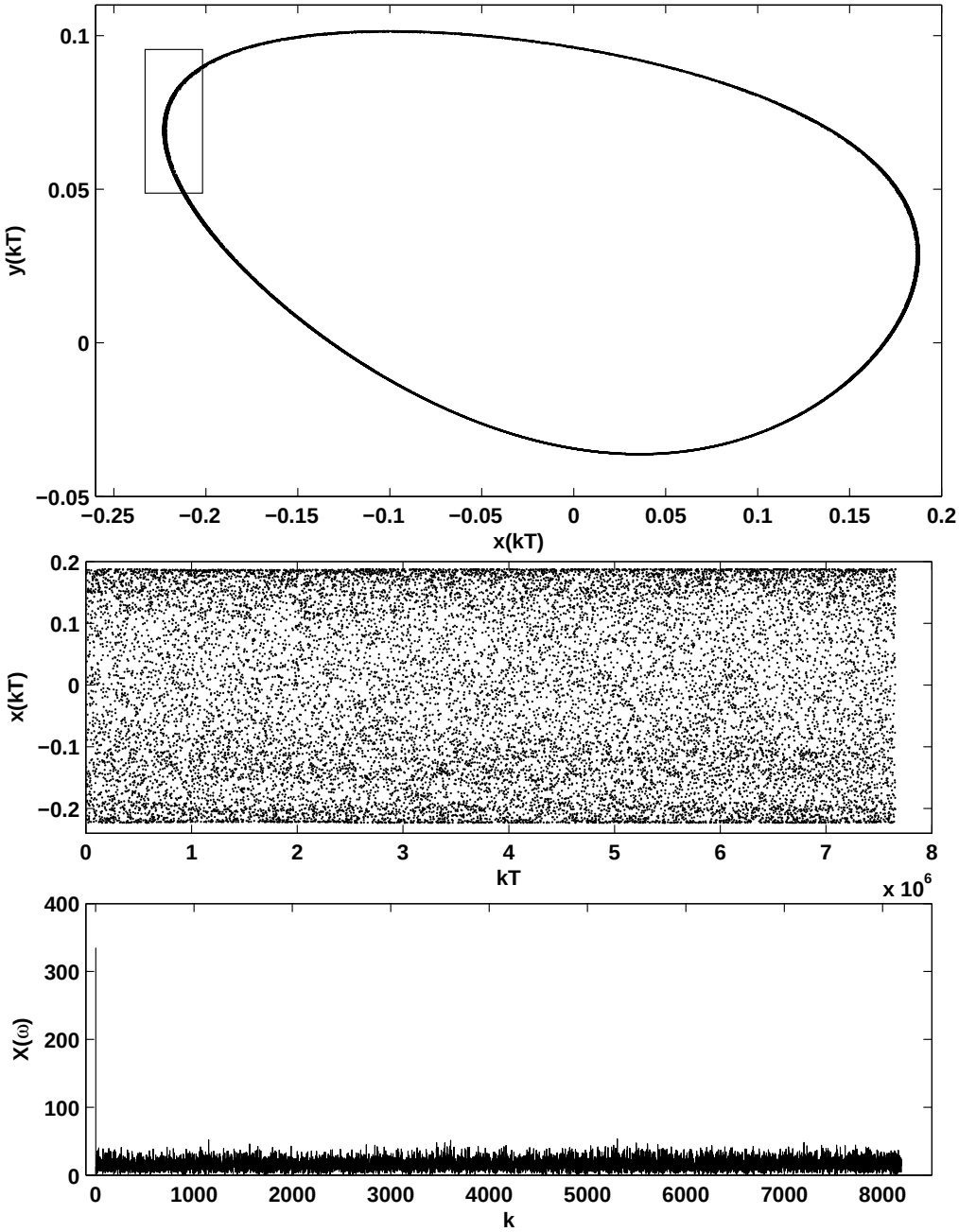

Figure 15: Strange attractor, $T = 467.0, \varepsilon_{11} = \varepsilon_{12} = \varepsilon_{13} = \varepsilon_{21} = \varepsilon_{22} = \varepsilon_{23} = 0.32$. Time-T map (top), $x(kT)$ versus kT (middle), frequency spectrum of $x(kT)$ (bottom).

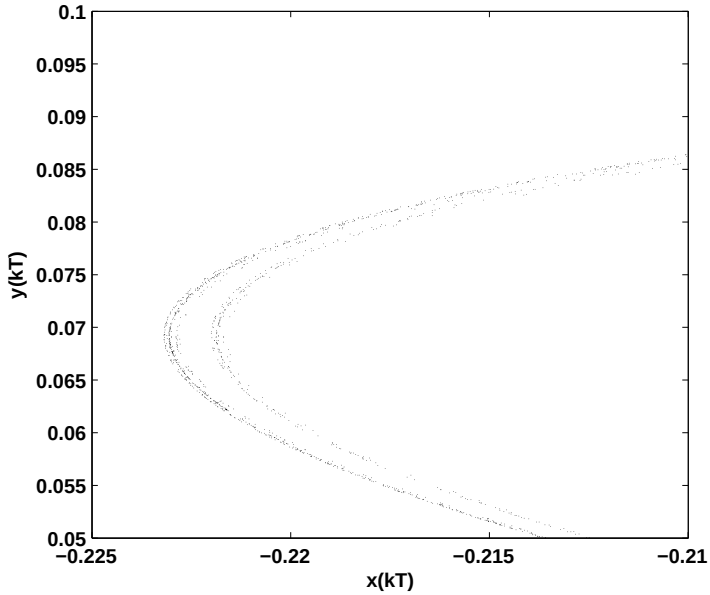

Figure 16: Local magnification of the indicated area of Fig. 15.

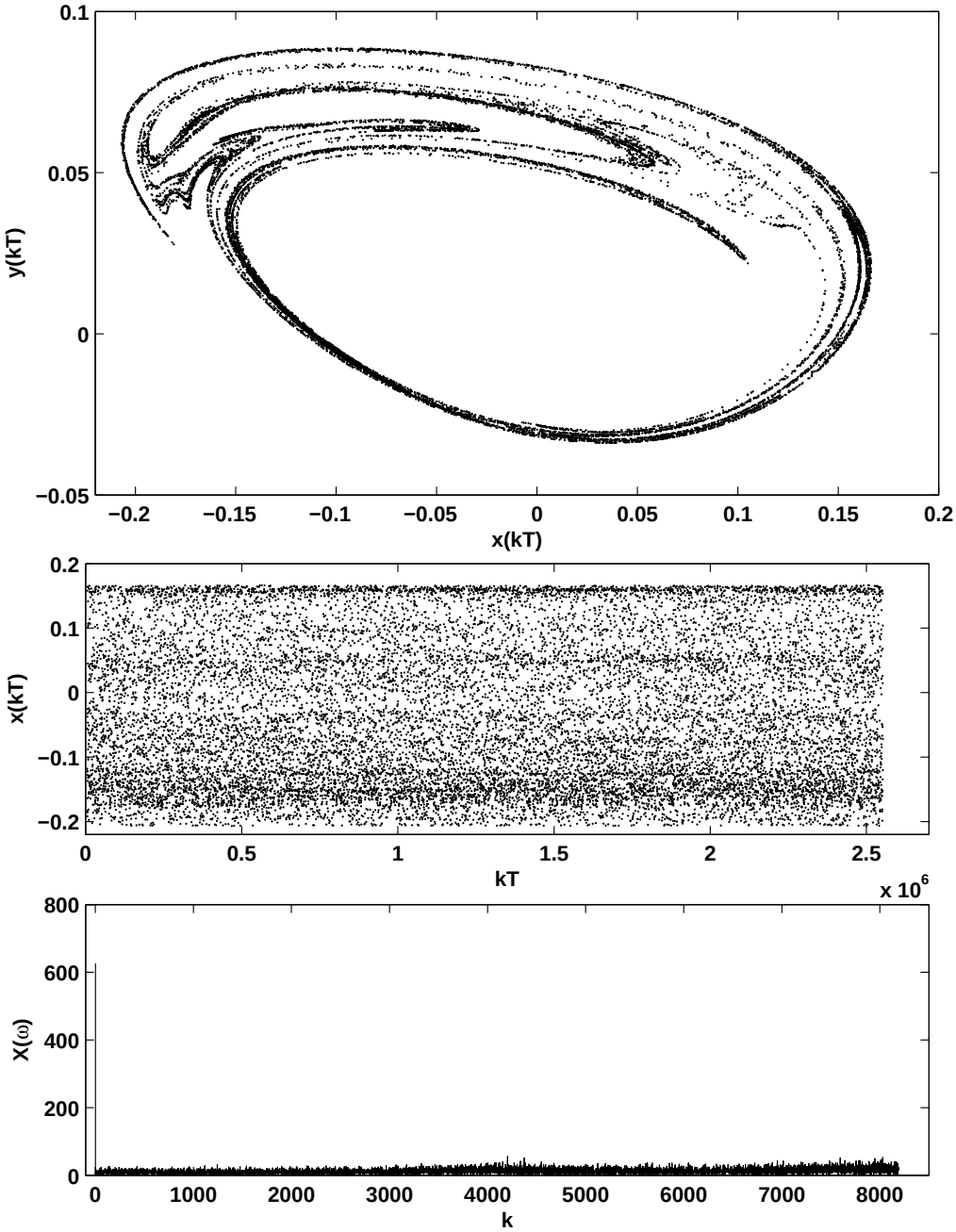

Figure 17: Strange attractor, $T = 155.5, \varepsilon_{11} = \varepsilon_{12} = \varepsilon_{13} = 0.22, \varepsilon_{21} = \varepsilon_{22} = \varepsilon_{23} = 0.12$. Time-T map (top), $x(kT)$ versus kT (middle), frequency spectrum of $x(kT)$ (bottom).

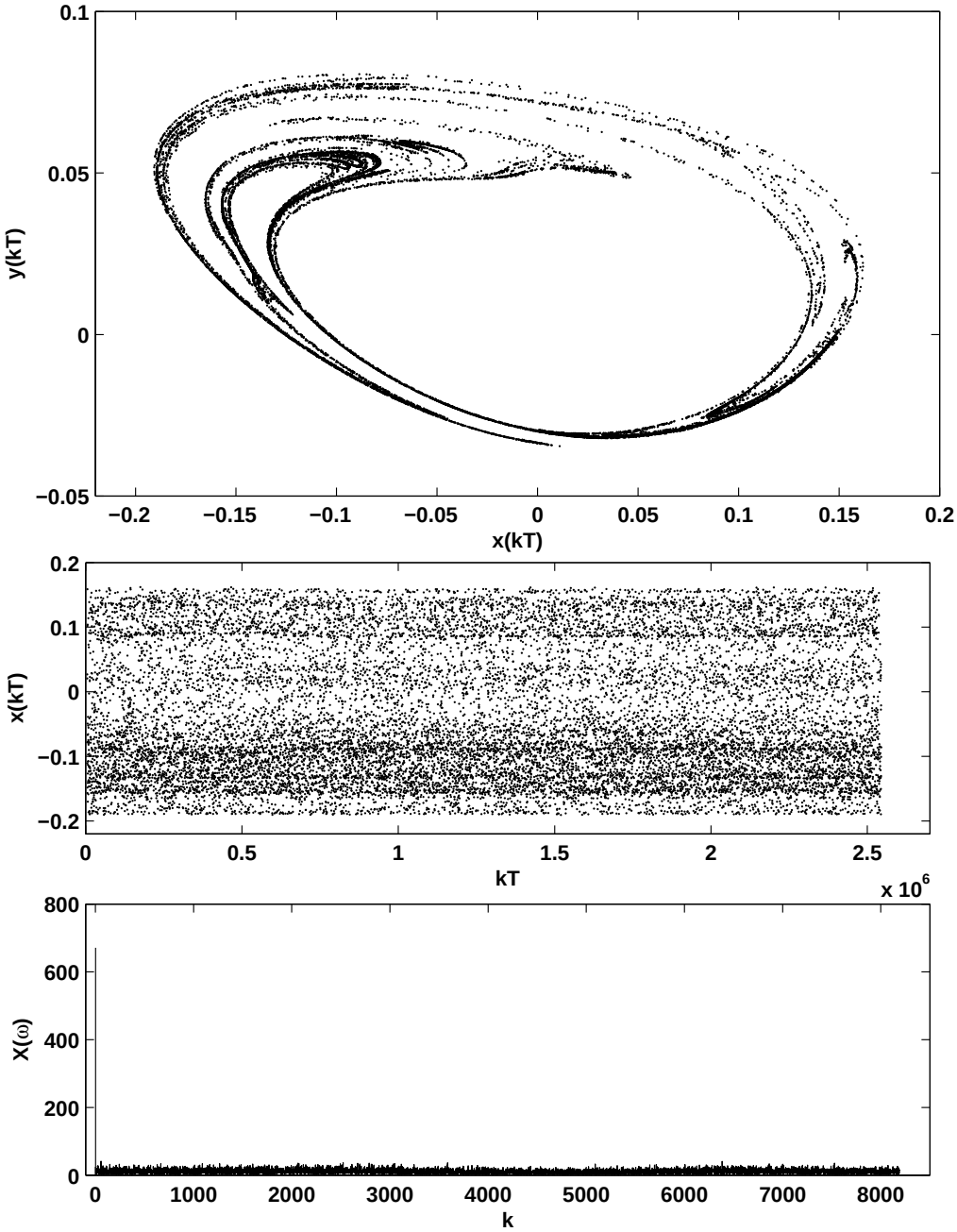

Figure 18: Strange attractor, $T = 155.0, \varepsilon_{11} = \varepsilon_{12} = \varepsilon_{13} = 0.12, \varepsilon_{21} = \varepsilon_{22} = \varepsilon_{23} = 0.22$. Time-T map (top), $x(kT)$ versus kT (middle), frequency spectrum of $x(kT)$ (bottom).

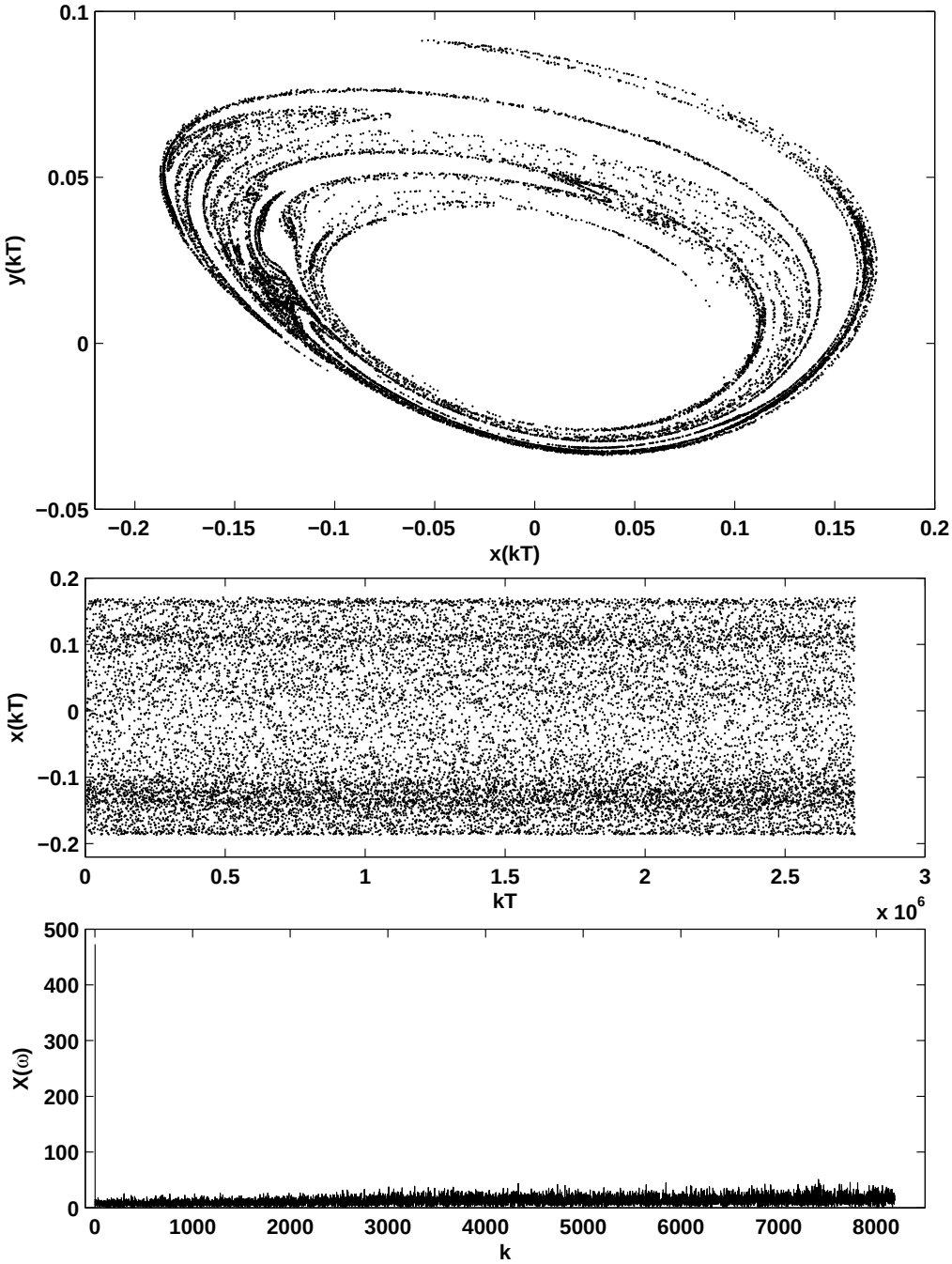

Figure 19: Strange attractor, $T = 167.5, \varepsilon_{11} = 0.12, \varepsilon_{12} = 0.52, \varepsilon_{13} = 0.12, \varepsilon_{21} = \varepsilon_{22} = \varepsilon_{23} = 0.22$. Time-T map (top), $x(kT)$ versus kT (middle), frequency spectrum of $x(kT)$ (bottom).

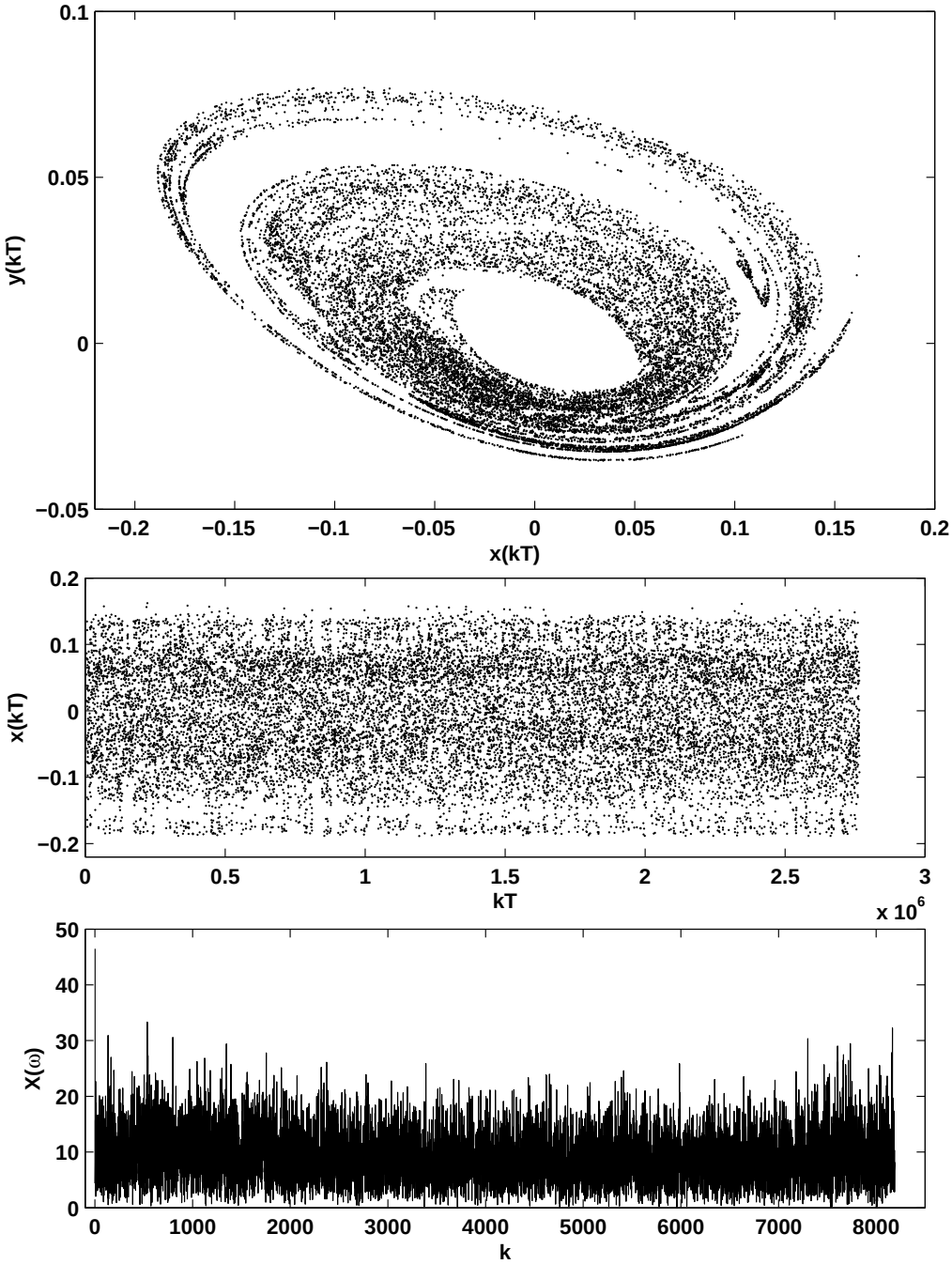

Figure 20: Strange attractor, $T = 168.5, \varepsilon_{11} = 0.12, \varepsilon_{12} = 0.52, \varepsilon_{13} = 0.12, \varepsilon_{21} = \varepsilon_{22} = 0.22, \varepsilon_{23} = 0.42$. Time-T map (top), $x(kT)$ versus kT (middle), frequency spectrum of $x(kT)$ (bottom).

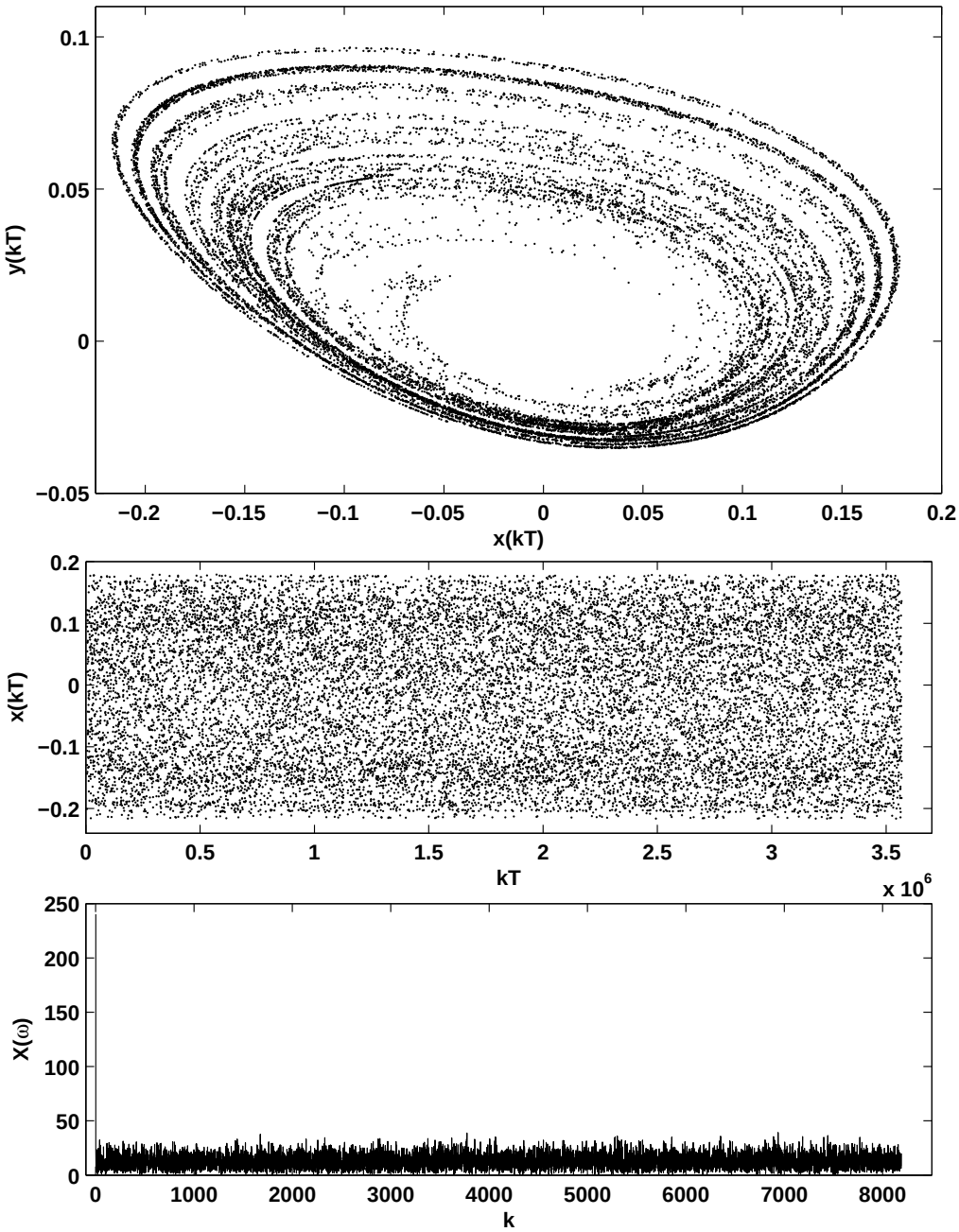

Figure 21: Strange attractor, $T = 217.0, \varepsilon_{11} = 0.32, \varepsilon_{12} = 0.52, \varepsilon_{13} = 0.12, \varepsilon_{21} = 0.22$, $\varepsilon_{22} = 0.32, \varepsilon_{23} = 0.42$. Time-T map (top), $x(kT)$ versus kT (middle), frequency spectrum of $x(kT)$ (bottom).

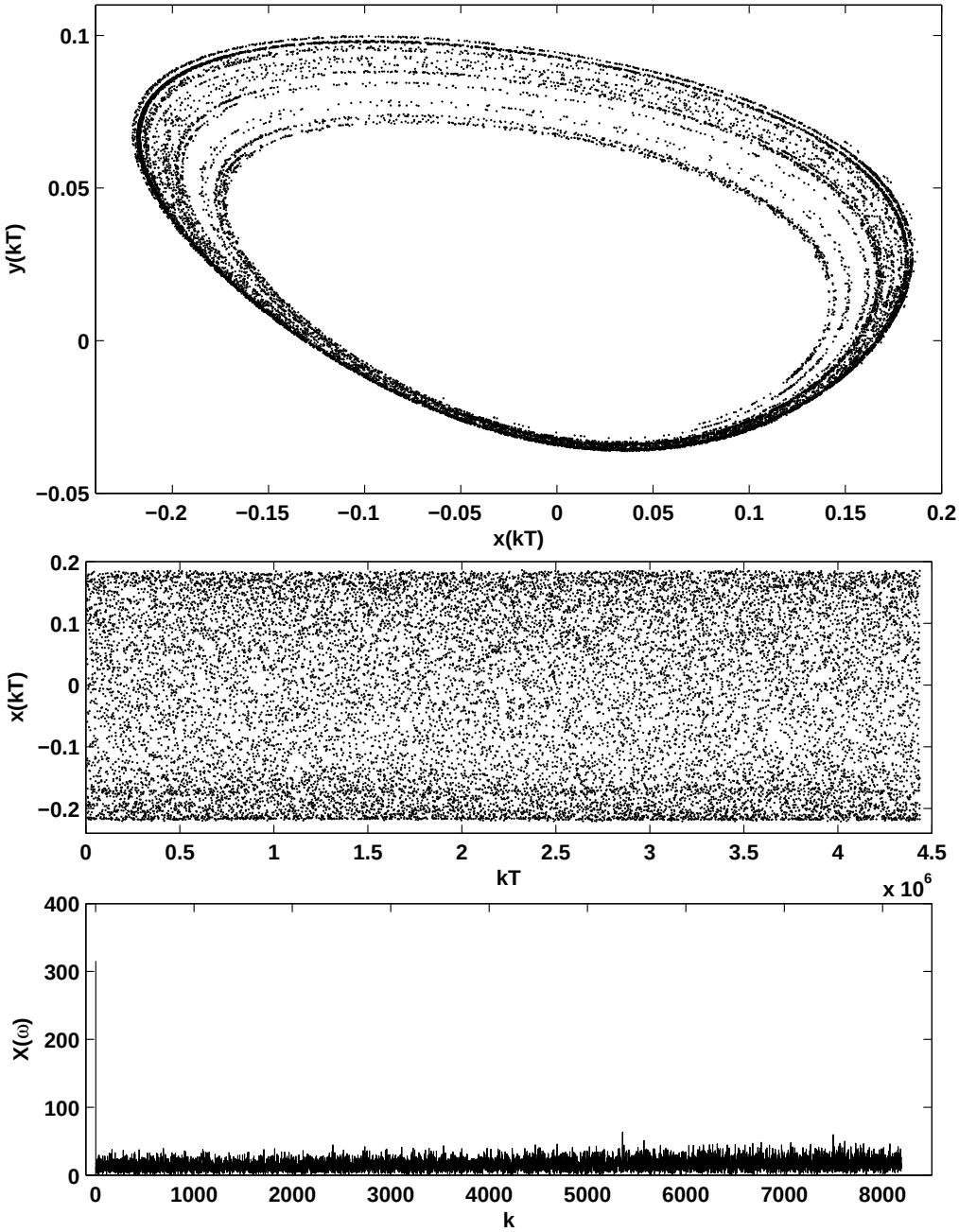

Figure 22: Strange attractor, $T = 270.5, \varepsilon_{11} = 0.32, \varepsilon_{12} = 0.52, \varepsilon_{13} = 0.12, \varepsilon_{21} = 0.22,$ $\varepsilon_{22} = 0.32, \varepsilon_{23} = 0.42$. Time-T map (top), $x(kT)$ versus kT (middle), frequency spectrum of $x(kT)$ (bottom).

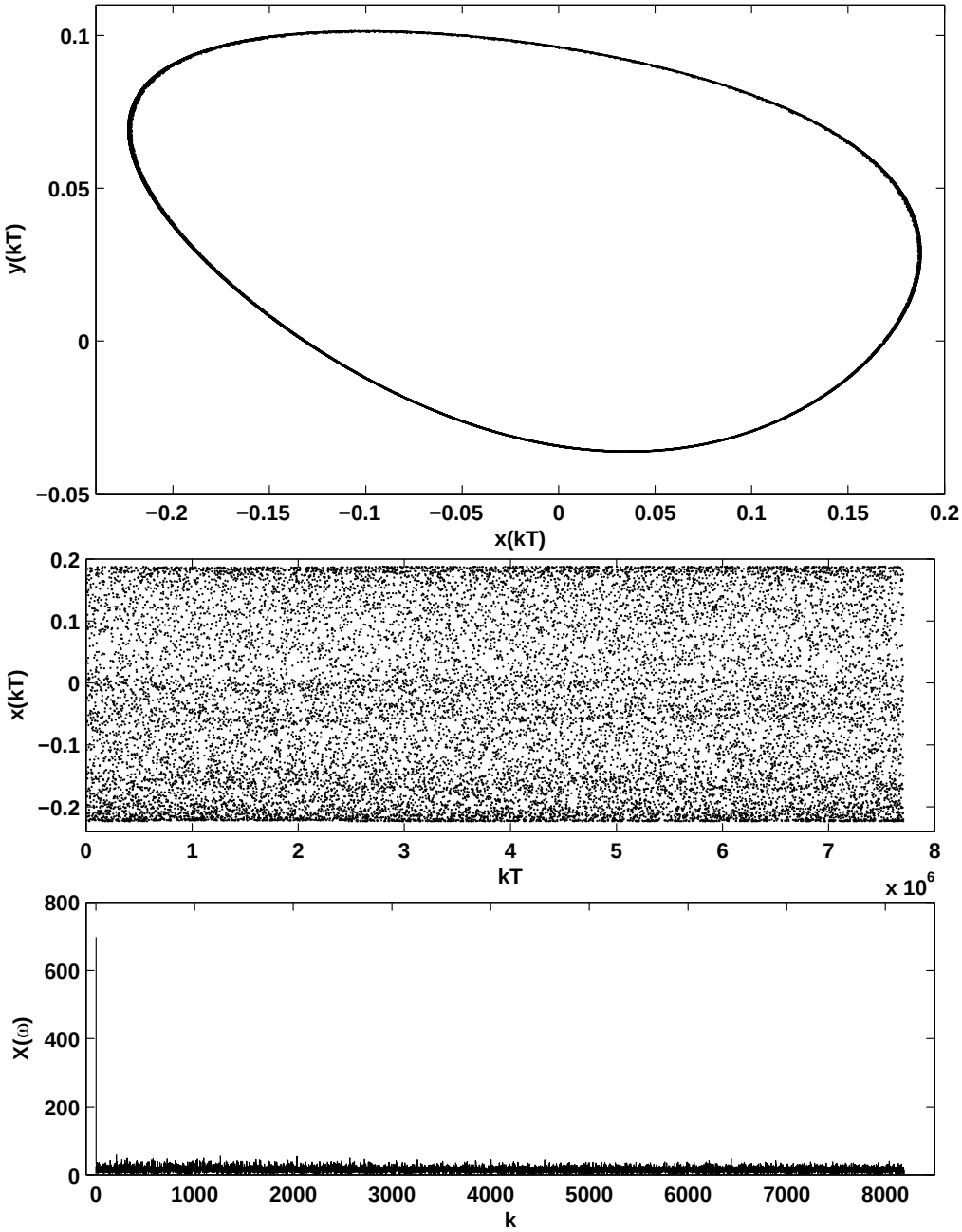

Figure 23: Strange attractor, $T = 470.0, \varepsilon_{11} = 0.32, \varepsilon_{12} = 0.52, \varepsilon_{13} = 0.12, \varepsilon_{21} = 0.22, \varepsilon_{22} = 0.32, \varepsilon_{23} = 0.42$. Time-T map (top), $x(kT)$ versus kT (middle), frequency spectrum of $x(kT)$ (bottom).

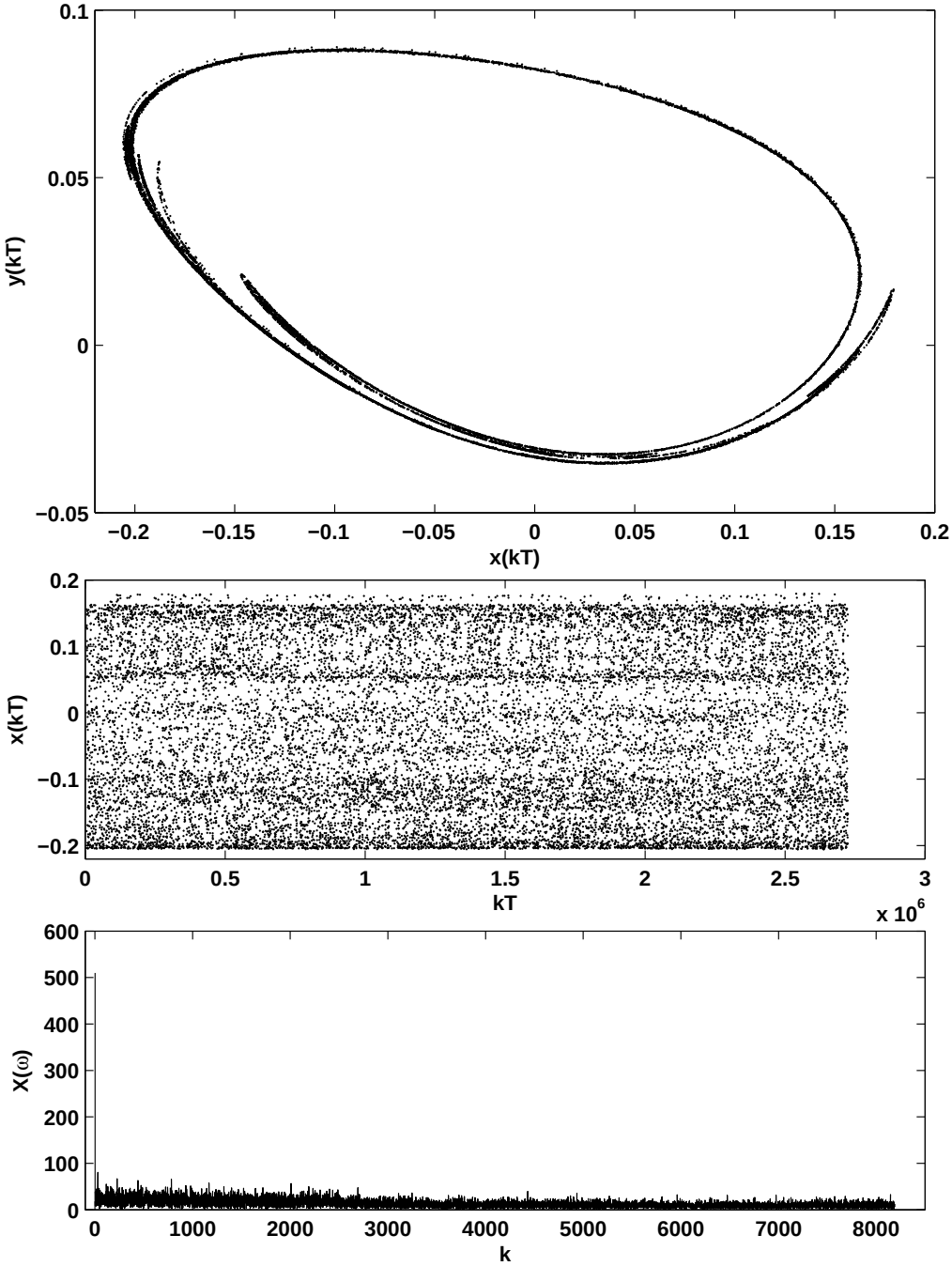

Figure 24: Strange attractor, $T = 166.0, \varepsilon_{11} = \varepsilon_{12} = \varepsilon_{13} = \varepsilon_{21} = \varepsilon_{22} = \varepsilon_{23} = 0.12$. Time-T map (top), $x(kT)$ versus kT (middle), frequency spectrum of $x(kT)$ (bottom).

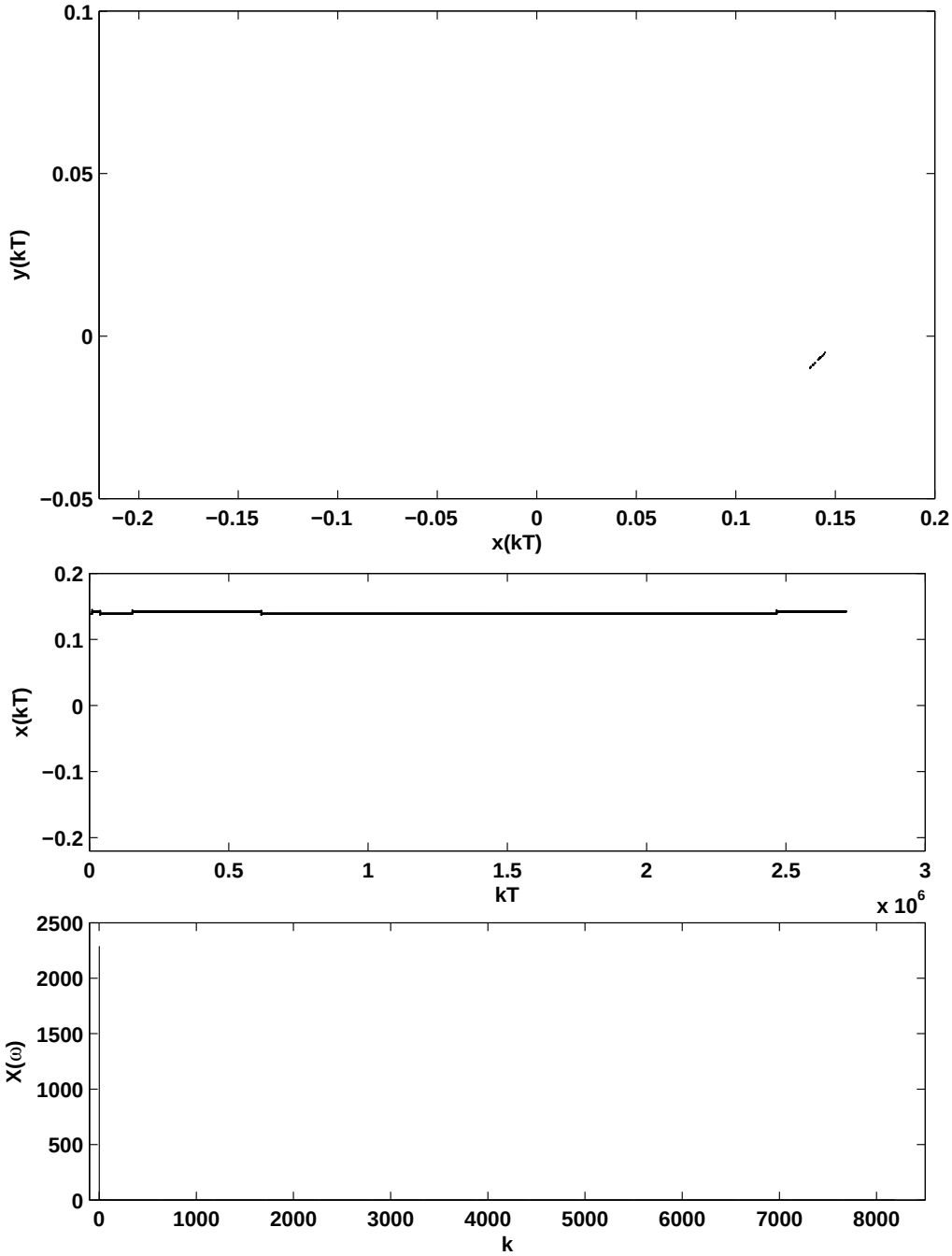

Figure 25: Periodic sink, $T = 165.5, \varepsilon_{11} = \varepsilon_{12} = \varepsilon_{13} = \varepsilon_{21} = \varepsilon_{22} = \varepsilon_{23} = 0.12$. Time-T map (top), $x(kT)$ versus kT (middle), frequency spectrum of $x(kT)$ (bottom).

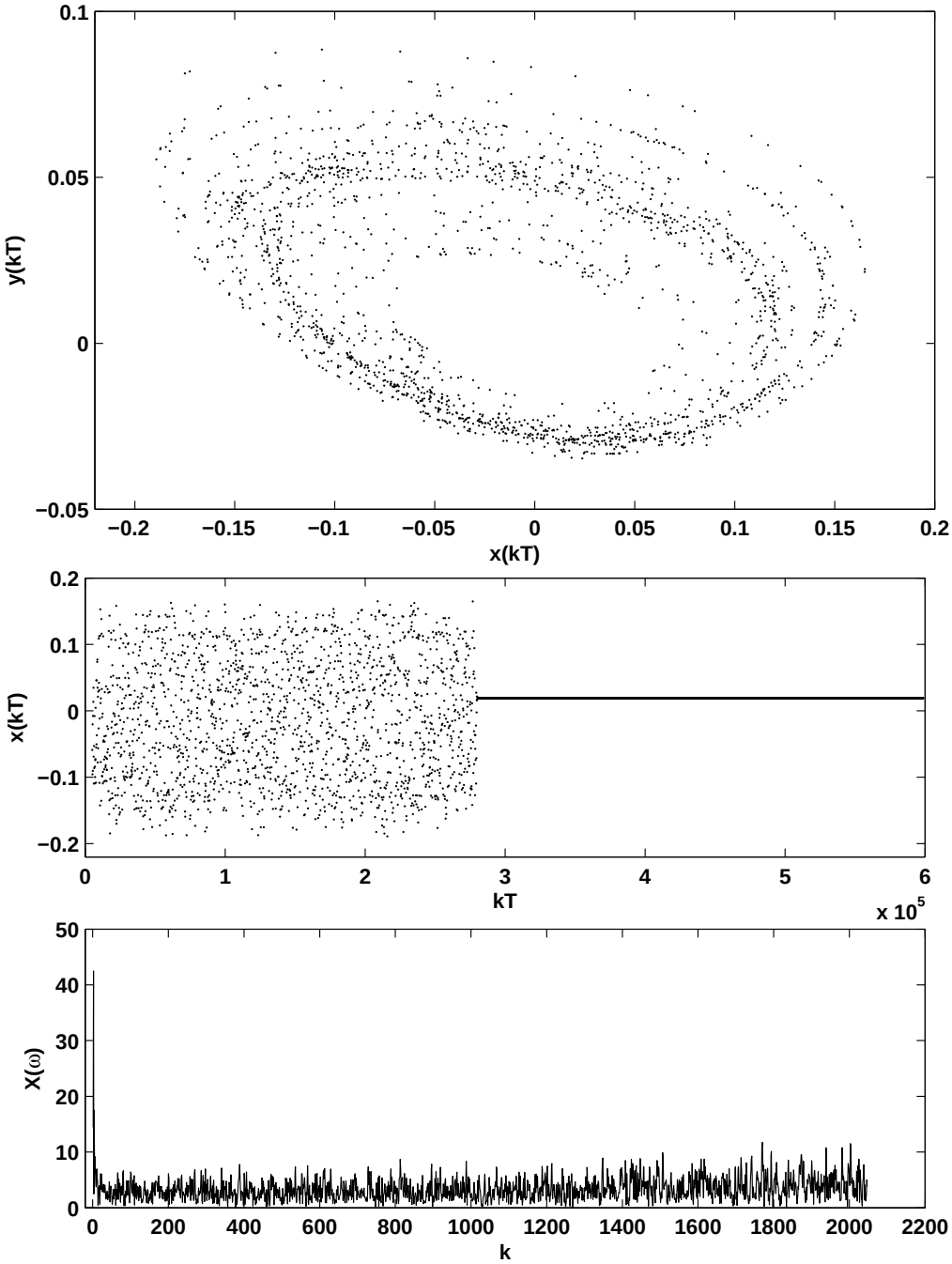

Figure 26: Transient chaos, $T = 145.0, \varepsilon_{11} = \varepsilon_{12} = \varepsilon_{13} = \varepsilon_{21} = 0.32, \varepsilon_{22} = \varepsilon_{23} = 0$. Time-T map (top), $x(kT)$ versus kT (middle), frequency spectrum of $x(kT)$ (bottom).

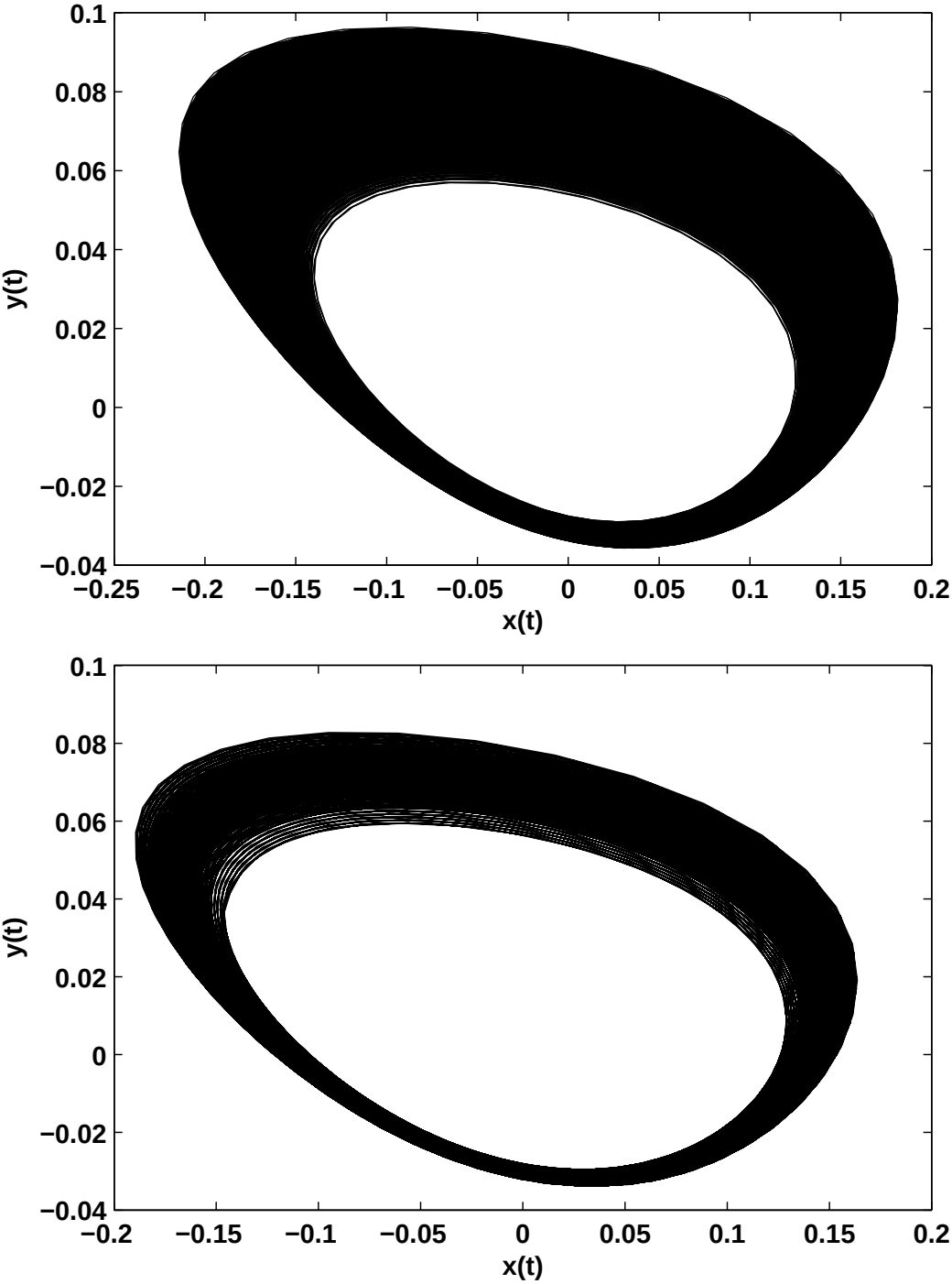

Figure 27: Two similar looking trajectories $\varepsilon_{11} = \varepsilon_{12} = \varepsilon_{13} = \varepsilon_{21} = \varepsilon_{22} = \varepsilon_{23} = 0.12$. Chaotic (from Fig. 24), $T = 166.0$ (top), Non-chaotic (from Fig. 25), $T = 165.5$ (bottom).